UPPSALA
UNIVERSITET

TVE 12056
Examensarbete 30 hp
December 2012

Salient Pole Motor Inverter Design

with Implementation of Space Vector Modulation

Anders Kronberg

Institutionen för teknikvetenskaper
Department of Engineering Sciences

UPPSALA
UNIVERSITET

Teknisk- naturvetenskaplig fakultet
UTH-enheten

Besöksadress:
Ångströmlaboratoriet
Lägerhyddsvägen 1
Hus 4, Plan 0

Postadress:
Box 536
751 21 Uppsala

Telefon:
018 – 471 30 03

Telefax:
018 – 471 30 00

Hemsida:
http://www.teknat.uu.se/student

Abstract

Salient Pole Motor Inverter Design with Implementation of Space Vector Modulation

Anders Kronberg

The researchers at the Department of Electricity at Uppsala University has recently entered the field of electric motor design, however no real knowledge of motor control of salient pole permanent magnet motors exists in the department. This master thesis is a continuation of a previous bachelor thesis that analyses the theory behind the control and simulating two different control methods. The two methods are here discarded for their high torque ripple. A third method is therefore implemented in this thesis to improve the performance.

This thesis will present the design and construction of an inverter for driving of a 30kW permanent magnet motor intended for vehicle propulsion. The work is divided into two parts, the power electronics and the control system hardware and software.

The results shows a working concept for a drive system, but further testing and improvements are needed to achieve maximum efficiency of the whole system.

Handledare: Boel Ekergård
Ämnesgranskare: Janaína Gonçalves de Oliveira
Examinator: Mikael Bergkvist
TVE 12056

Sammanfattning

Ett drivsystem för högeffektiva elektriska fordonsmotorer har konstruerats och testats på en 30kW motor utvecklad på Uppsala universitet. Resultaten visar att systemet fungerar, men att det även finns behov av förbättringar.

Med tanke på de senaste årens forskning och debatt om peak oil och en ökande mängd växthusgaser i atmosfären har det blivit tydligare att världens energikonvertering måste förändras för ett mer hållbart samhälle. Avdelningen för elektricitetslära på Uppsala universitet har det senaste decenniet fokuserat på utveckling av förnyelsebara energikällor, så som vind-, våg-, vatten- och marin strömkraft. Med samma verktyg och metoder som använts vid utvecklingen av högeffektiva generatorer har de nyligen gett sig in på området elektriska motorer för fordonsframdrift.

En av elbilens nackdelar är dess räckvidd, för att kunna konkurrera med dagens bilar är det därför viktigt att optimera verkningsgraden i de olika delsystemen mellan laddkontakt och hjul. I detta arbete presenteras en metod i vilken de tre fasernas drivelektronik styrs som en enhet istället för att behandla den som tre oberoende enheter. Detta möjliggör en 15.4% högre drivspänning till motorn, vilket leder till lägre strömmar och förluster för samma uteffekt.

Arbetet omfattar konstruktion av kraftelektronik, styrelektronik och programmering av styrelektroniken, samt test och verifiering av hela systemet.

Contents

List of Figures

Nomenclature

C	Capacitance
L	Inductance
P_{elm}	Electromagnetic power
P_{in}	Input power
Q	Electric charge
R	Resistance
T_e	Electromagnetic torque
V_{nN}	Common mode voltage
λ	Flux linkage
λ_{pm}	Flux linkage per phase from permanent magnets
ω_e	Electrical rotational speed
ω_m	Mechanical rotational speed
θ	Mechanical angle
f	Frequency
h_{FE}	Transistor amplification factor
i	Current
v	Voltage

Denominators

A, B, C	Inverter phase denominators
CE	Collector Emitter
GC	Gate Collector
GE	Gate Emitter
a, b, c	Load phase denominators
d	Direct axis denominator
g	gate
h	High switch
l	Low switch
n	Normalized value
q	Quadrature axis denominator
s	Stator

Nominators

*	Reference value

Abbreviations

AC	Alternating Current
BJT	Bipolar Junction Transistor
BLDC	BrushLess Direct Current motor
CT	Current Transformer
DC	Direct Current
DSP	Digital Signal Processor
DTC	Direct Torque Control
FOC	Field Oriented Control
FPGA	Field Programmable Gate Array
HECS	Hall Effect Current Sensor
HMI	Human Machine Interface
IGBT	Insulated Gate Bipolar Transistor
IM	Induction Motor
MCU	Micro Controller Unit
MOSFET	Metal Oxide Semiconductor Field Effect Transistor
MTPA	Maximum Torque Per Ampere
NSPMSM	Negative Saliency Permanent Magnet Synchronous Motor
PMAC	Permanent Magnet Alternating Current motor
PMSM	Permanent Magnet Synchronous Motor

PSPMSM Positive Saliency Permanent Magnet Synchronous Motor

SPMSM Surface mounted Permanent Magnet Synchronous Motor

SPWM Sinusoidal Pulse Width Modulation

SVM Space Vector Modulation

VFD Variable Frequency Drive

bemf Back ElectroMotive Force

ppr Pulses Per Revolution

Chapter 1

Introduction

1.1 Introduction

This thesis presents the work towards the construction of an inverter for a Permanent Magnet Synchronous Motor (PMSM). An inverter is a variable frequency drive that is needed to be able to run a synchronous motor with variable speed. The work consists of design and construction of both the power electronics and the control system.

1.2 Background

With the recent years research and debates about an increasing level of greenhouse gases and peak oil, it has become clearer that a change in worlds the energy conversion is needed. The Department of Electricity at Uppsala University has for the last decade focused on the development of renewable electricity sources, such as wind-, wave-, hydro- and marine current power as a way for a more sustainable society. Recently, research regarding high efficiency electric motors has been included in the department's research.

PMSM has because of their small size and high performance, been used for a long time in industrial applications such as servo motors and lately they have started to become popular as larger drive motors. This has been made possible by the introduction of modern magnetic materials, such as Neodymium Iron Boron and Samarium Cobalt. These types of magnets have a higher energy density and are less susceptible for demagnetizing. Another large market for PMSM will probably be electric vehicles, where the motors size, performance and weight give it an advantage over DC- and Induction Motors (IM)[1].

1.3 Purpose

The purpose of this thesis has been to design and build an inverter concept that can be used to include our new motor design into our flywheel based all-electric driveline[2]. The work done is a continuation of a previous bachelors thesis, the simulations done in "Design and Simulation of Field Oriented Control and Direct Torque Control for a Permanent Magnet Synchronous Motor with Positive Saliency"[3] was showing a high torque ripple. One of the goals for this thesis has therefore been to implement a more sophisticated control method to reduce the torque ripple.

1.4 Thesis Outline

Chapter 2 presents some basic inverter theory and background information on potential components for the inverter, it also presents the theory of the space vector modulation control algorithm. Chapter 3 presents the component selection and construction of one small and one large inverter, whereas chapter 4 presents the control algorithm implementation in the control system. Chapter 5 presents the testing and results of the large inverter, and chapter 6 discusses the construction work and the results. Chapter 7 concludes the work and presents a suggestion of future work to be done. Appendix A gives an instruction for configuring and assembling the IGBT drivers.

Chapter 2

Theory

2.1 Introduction

Choosing the correct components for an inverter drive can be a complicated task, the reason of this chapter is therefore to present some very basic theory and functionality of components that could be used. The components presented is the motor, power electronics, control system, position- and current sensors. It will also present the control theory for permanent magnet motors and space vector modulation.

2.2 Permanent Magnet Motors

2.2.1 Introduction

The PMSM is a synchronous AC motor, normally constructed with a three phase stator winding similar to conventional Induction Motors. The big difference between them is in the rotor. In the IM the rotor is magnetized by a current induced in the cage of conducting bars located in the rotor. To induce this current there has to be a difference in speed between the rotor and the stators rotating field, this has given the motor its other name: The Asynchronous Motor. For PMSM permanent magnets is used to provide a constant flux to magnetize the motor. The lack of an electrical excitation system gives the PMSM lower losses and higher efficiency compared to IM or separately exited synchronous motors.

The PMSM can be divided in to two categories depending on the armature winding distribution, BrushLess DC (BLDC) and Permanent Magnet AC (PMAC). BLDC has a short winding distribution than span only a fraction of the pole pitch ($\ll 180°$), this gives the motor a trapezoidal back emf[4]. The PMAC has windings that spans close to the pole pitch ($\approx 180°$), this gives the motor a sinusoidal back emf[4].

To be able to run the PMSM with variable speed an inverter is needed. A correctly chosen inverter is capable of supplying the motor with a variable frequency and voltage level for the whole operating range.

Torque production

The electrical input power of a three phase electric machine can be described by

$$P_{in,abc} = v_a i_a + v_b i_b + v_c i_c \tag{2.1}$$

where v is the phase voltage, i the phase current and $_{abc}$ denotes the phase. Applying the transformation of motor parameters described on page 18 it can be described in a dq

reference frame as

$$P_{in,dq} = \frac{2}{3}(v_d i_d + v_q i_q). \tag{2.2}$$

Where the d and q voltages is described by

$$v_d = R_s i_d + \frac{d\lambda_d}{dt} - \omega_e \lambda_q \tag{2.3}$$

$$v_q = R_s i_q + \frac{d\lambda_q}{dt} + \omega_e \lambda_d \tag{2.4}$$

and the flux linkages is described by

$$\lambda_d = L_d i_d + \lambda_{pm} \tag{2.5}$$

$$\lambda_q = L_q i_q. \tag{2.6}$$

Where L_d and L_q is the d and q axis inductances, λ_{pm} is the flux linkage per phase generated from the permanent magnets, R_s is the stator resistance and ω_e is the electrical rotational frequency. The input power has to be equal to output power, which gives

$$\frac{3}{2}(v_d i_d + v_q i_q) = \omega_e \frac{3}{2}(\lambda_d i_q - \lambda_q i_d) + \frac{3}{2}\left(R_s i_d^2 + \frac{d\lambda_d}{dt} i_d + R_s i_q^2 + \frac{d\lambda_q}{dt} i_q\right) \tag{2.7}$$

where the term $\omega_e(\lambda_d i_{sq} - \lambda_q i_{sd})$ accounts for the electromagnetic power P_{elm}

$$P_{elm} = \omega_e \frac{3}{2}(\lambda_d i_{sq} - \lambda_q i_{sd}) \tag{2.8}$$

or

$$P_{elm} = \omega_e \frac{3}{2}\left[\lambda_{pm} i_q - (L_q - L_d) i_d i_q\right]. \tag{2.9}$$

The electromagnetic torque for a three phase motor with p poles is then described by[5]

$$T_e = \frac{3}{2}\frac{p}{2}\left[\lambda_{pm} i_q - (L_q - L_d) i_d i_q\right]. \tag{2.10}$$

2.2.2 Saliency

Saliency is a measure of the non-symmetry of the motors magnetic properties created by a difference in reluctance for different magnetic paths. This difference arises from variation in the rotors material or its geometry and it will show itself as a difference in the motors inductance parameters L_d and L_q. A motor can be positive-, negative- or non-salient.

The definition and naming convention of saliency is not very well defined[3], in this paper the definition from "Design and Simulation of Field Oriented Control and Direct Torque Control for a Permanent Magnet Synchronous Motor with Positive Saliency is used"[3]. The definition originates from a traditional electrically exited synchronous machine and its electromagnetic properties, which has been considered to have normal or positive saliency.

- PSPMSM - Positive Saliency Permanent Magnet Synchronous Motor.
  Rotor type where $L_d > L_q$.
- NSPMSM - Negative Saliency Permanent Magnet Synchronous Motor.
  Rotor type where $L_d < L_q$.
- SPMSM - Surface mounted Permanent Magnet Synchronous Motor.
  Rotor type where $L_d = L_q$.

2.2.3 Rotor Designs

There is many different designs of PMSM rotors, some common types are shown in figure 2.1. Magnets can be mounted either on the surface or internally of the rotor, the steel part of the rotor can be either solid or built up by thin layers of steel plates. Surface mounted magnet rotors are easy to construct, but they will not be good for high rotational speed where the magnets are prone to separate or crack by the centrifugal forces. An internal magnet rotor protects the magnets from mechanical stress, but the magnets have to be isolated by slots or non-magnetic material to prevent a magnetic path to form internally in the rotor. The magnetic path has to be through the stator around the armature windings to be effective.

Rotors with buried magnes are illustrated in figure 2.1a, 2.1b, 2.1e, 2.1f and 2.1j.

Figure 2.1a and 2.1f show rotors with damper windings, the winding gives the ability to start the motor asynchronously and also dampening oscillations.

Figure 2.1g and 2.1h show rotors with rounded magnet, which gives a more sinusoidal field distribution with less harmonics[6].

A rotor with surface mounted magnets such as figure 2.1c, 2.1g, and 2.1h has a wide **magnetic** air gap, resulting in a low magnetizing inductance with difficulty to influence the motors electromagnetic properties from the stator current. These rotors have no saliency due to the low permeability value of the magnets. By utilize buried magnets the **magnetic** air gap can be reduced, and a higher magnetizing inductance can be found, giving an increased controllability of the electromagnetic properties from the stator current. An opportunity to extend the motors speed range beyond the base speed by controlling the stator current in a way that the flux reduces thus decreasing the back electromotive force (bemf) for a certain speed is therefore found.[7]

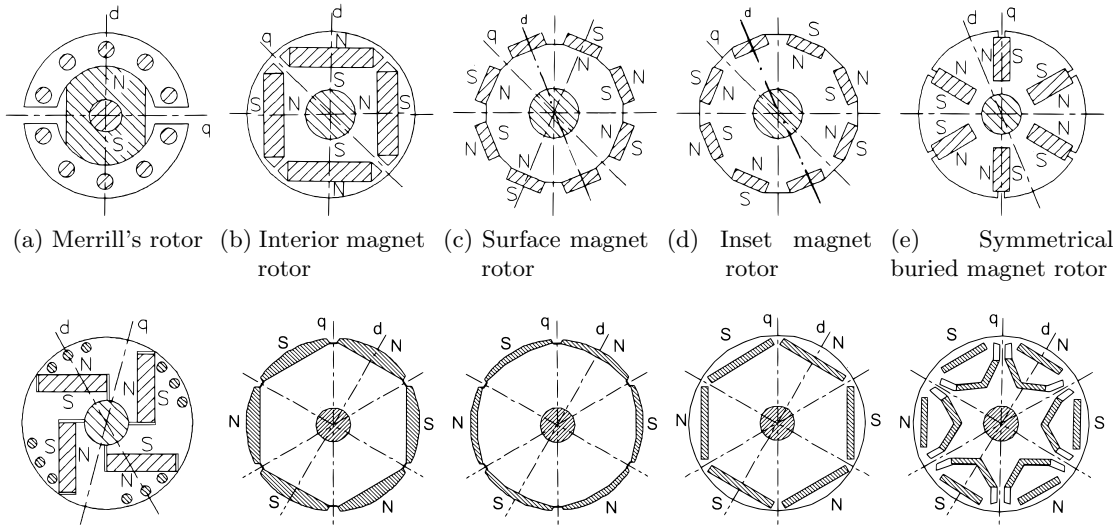

(a) Merrill's rotor (b) Interior magnet rotor (c) Surface magnet rotor (d) Inset magnet rotor (e) Symmetrical buried magnet rotor

(f) Asymmetrical buried magnet rotor (g) Bread loaf magnet rotor (h) Decentered magnet rotor (i) Interior magnet six pole rotor (j) Interior double layer magnet rotor

Figure 2.1: Different types of rotor configuration.[1]

[1]Permanent magnet motor technology: design and applications, Jacek F. Gieras

2.2.4 The Boel Motor

The motor used in this work is a cable wound, two pole, high speed, high efficiency motor developed at Uppsala University. The motor is designed for use with a 2:1 differential gear or direct drive with small vehicular wheels in mind.

The development of electric propulsion systems by car manufacturers has mostly been focused on four, six or eight pole motor with a poor efficiency below 95%. However, with the solution of Maxwell's equations it is realized that for high speed drives, the smaller amount of poles the more compact and cost effective the motor will be. Simulations show an efficiency between 95-98% through the operating range.[8]

The motor is a downscaled version of a 1.6GW nuclear turbo generator with a permanent magnet rotor and cable wound stator. The rotor is of simple construction with a permanent magnet sandwiched between the two iron poles bolted together with the rotor end plates illustrated in figure 2.2.

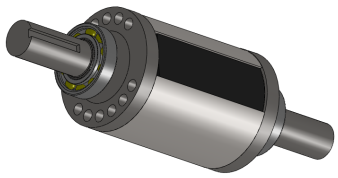

Figure 2.2: Two Pole Permanent Magnet Rotor.

A Cable wound stator give a uniform electrical and magnetic field, which utilizes the insulation material as good as possible, compared to square windings which have higher electrical stress in the corners. The use of cables gives the possibility to use higher voltage and lower currents for the same power, thus reducing copper losses in the windings.[9]

The motors most important parameters from a control perspective can be seen in table 2.1

Table 2.1: Motor parameters.

$V_{rated,LL,rms}$	$260V$	R_s	0.015Ω	p	2
ϕ	3	L_d	$4mH$	rpm	$0-3000$
$I_{rated,rms}$	$49A$	L_q	$1mH$	J_{est}	$0.003334kgm^2$
I_{max}	$100A$	$\lambda_{pm,fullload}$	$0.1960Wb$	F_{est}	$0.00425Nms$
P_{rated}	$30kW$				
P_{max}	$60kW$				

where $V_{rated,LL,rms}$ is the rated line voltage, ϕ is the number of phases, $I_{rated,rms}$ and I_{max} is the rated and maximum current, P_{rated} and P_{max} is the rated and maximum phase current, R_s is the stator inductance, $\lambda_{pm,fullload}$ is the magnetic flux from the rotor magnets, p is the number of poles, rpm is the speed range, J_{est} is the estimated inertia of the rotor, and F_{est} is the estimated friction.

2.3 Sensors

2.3.1 Current Sensors

Shunt

By placing a well known resistor in series with the load and measuring its voltage drop, the current can be calculated from Ohm's law

$$I = \frac{U}{R}. \tag{2.11}$$

The power loss in the resistor needs to be low and therefore the resistance is kept low, thus giving a very low voltage drop. The low voltage makes the circuit more sensitive for interference and the voltage needs to be amplified to usable levels. The output value should also be galvanic isolated from any high voltage circuits.

Transformers

The Current Transformer (CT) provides galvanic isolation and steps down the voltage from the measured primary winding to the output secondary winding. To the secondary winding a resistor is connected and the voltage drop is measured and the current is calculated from Ohm's law and the transformers winding factor. A disadvantage of using CT is that they only can measure AC currents and that they have a limited frequency range

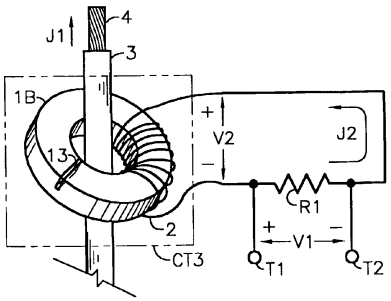

Figure 2.3: Current Transformer.[2]

Hall Effect

Hall Effect Current Sensors (HECS) working principle is to measure the magnetic field around a conductor with a hall effect sensor. The sensor is placed between the ends of an open soft magnetic core and gives a voltage proportional to the current. The measured cable is routed through the core or wound around it to achieve an amplification of the measured current. The hall sensor output voltage is very low and need to be highly

[2] http://4hv.org/e107_files/public/1329801792_1403_FT1630_6954060-0-large_.jpg

amplified, in commercial HECS this is done internally in the sensor housing. The HECS can unlike the CT measure DC current and high frequencies if a suitable core material is used. Disadvantages is that the sensors tend to have DC offset voltage at zero current and that high current peaks can permanently magnetize the core and introduce a bigger DC offset voltage.

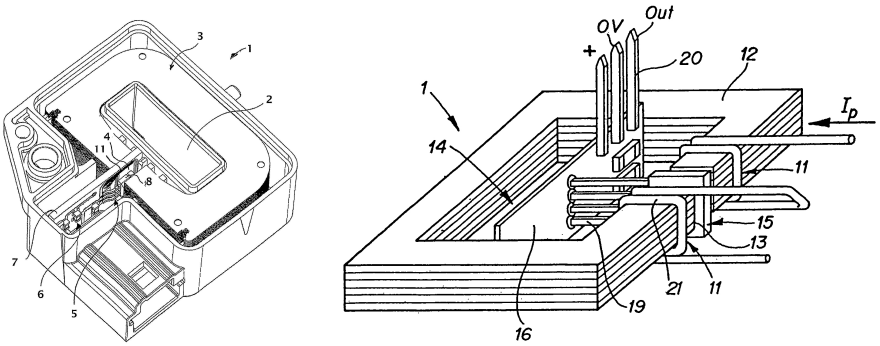

(a) Open Loop (b) Closed Loop

Figure 2.4: Hall Effect Current Sensors.[3]

There exist two types of sensors, open loop and closed loop. The open loop is described above and can be seen in figure 2.4a, where (3) is the core and (8) is the hall effect sensor. In the closed loop current sensor seen in figure 2.4b, the voltage from the hall sensor (15) is amplified and feed into a secondary compensating winding (11) around the core (12). The secondary winding creates a flux of the same magnitude but with opposing direction compared to the primary measured current, cancelling the flux in the core. Any nonlinearities and temperature dependencies are therefore eliminated. [10]

2.3.2 Position Sensors

Hall Effect

Discrete hall effect sensors are often used in BLDC application where the sensors are placed with 120° electrical displacement. This gives a possibility to easily determine to which sector the rotor poles is oriented, this knowledge is enough to drive a BLDC motor with a square wave commutation scheme.

Linear hall effect sensors are not using the rotor magnets a position reference, instead they use a ordinary magnet attach to the end of the shaft. Depending on the magnets angle it displaces the current through the sensor differently and the sensor outputs a voltage that is linearly dependent of the magnets angle.

Incremental Quadrature- and Absolute Encoders

The encoders are based on an optical detector where light shines through a patterned disc onto a photo diode on the opposite side. The discs are manufactured from plastic or steel depending of the required temperature range.[11]

The absolute encoders give an absolute position by patterning the disc with gray code, binary code or Binary Coded Decimals (BCD). Increasing the resolution is done by

[3](a) - US Patent No. 7,977,934 B2, (b) - US Patent No. 7,193,408 B2

adding another bit pattern to the outside of the disc, quickly increasing the complexity and decreasing the size of the window in the disc as the resolution goes up. For reading the disc one photo diode for every bit is needed and the encoder outputs a bit pattern that repeats once for every revolution.[11]

The incremental encoder only uses one layer of windows and two photodiodes with 90° displacement, thus making it a simpler construction then the absolute encoder. The drawback is that the encoder does not remember its position since the information is not hardcoded in the disc, the encoder only outputs two square wave signals displaced 90° that has to be processed by hardware/software to get the position. Most encoders also has a third output with one pulse per revolution, it can function as a reference or sync pulse in case missed pulses.[11] Figure 2.5 shows three different encoding options for an

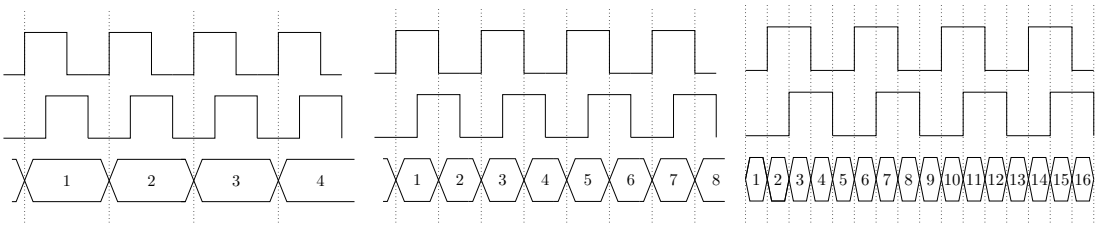

(a) X1 encoding. (b) X2 encoding. (c) X4 encoding.

Figure 2.5: Different encoding types.

incremental encoder. X1 counts periods, X2 counts pulses and X4 counts flanks. By changing the encoding the resolution of the encoder can be changed. The angle can be calculated from

$$\theta^\circ = \frac{count}{Xppr} 360^\circ \tag{2.12}$$

where *count* is the number of counts recorded, X is the encoding type and ppr is the number of pulses per revolution.[12]

2.4 Inverters

2.4.1 Introduction

The main purpose of an inverter is to create an Alternating Current (AC) from a Direct Current (DC) source. The inverter makes it possible to drive an AC motor from a DC source, or drive the motor with a different frequency than the electric grid. It also makes it possible to feed energy from a DC source to the electric grid, such as from photovoltaic cells or wind turbines with a battery energy storage. A two level three phase inverter is constructed from three legs, A, B and C. Each is connected to a separate phase of the load, a, b and c. The switches is usually MOSFET or IGBT, they are operated complementary and depending on if the upper (X_h) or lower switch (X_l) is closed the leg voltage (V_X) can be either $+V_{DC}$ or 0. By turning the switches on and off in a defined sequence it is possible to create a time varying output voltage for different waveforms.

The leg voltage as a function of the high side switch position can be described as

$$\begin{cases} V_A = S_{A_h} V_{DC} \\ V_B = S_{B_h} V_{DC} \\ V_C = S_{C_h} V_{DC} \end{cases} \tag{2.13}$$

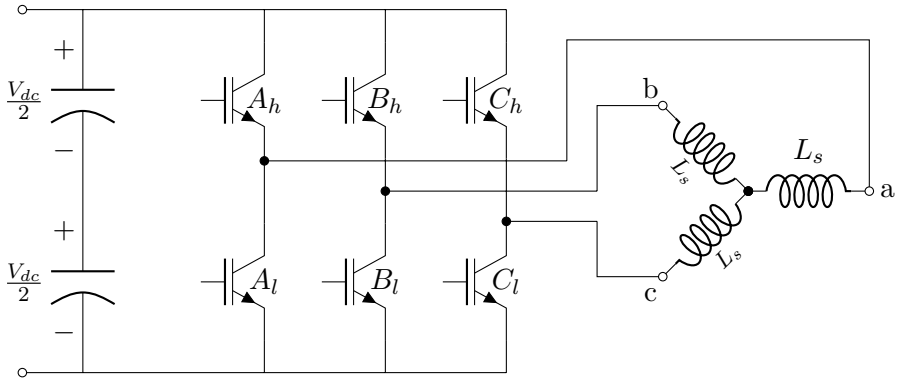

Figure 2.6: Two level inverter connected to an ideal three phase motor model.

where $S_X = 1$ indicates the top switch X_h is closed and $S_X = 0$ indicates the bottom switch X_l is closed.[13] For a three phase Y-connected load the loads phase voltages V_X can be written as

$$\begin{cases} V_A(t) = V_a(t) + V_{nN} \\ V_B(t) = V_b(t) + V_{nN} \\ V_C(t) = V_c(t) + V_{nN} \end{cases} \tag{2.14}$$

where V_{nN} is the voltage difference between the loads center point and negative side of the DC-bus. Assuming a balanced load the sum of the phase voltages is zero

$$V_a(t) + V_b(t) + V_c(t) = 0 \tag{2.15}$$

which gives

$$V_{nN}(t) = \frac{1}{3}V_A(t) + V_B(t) + V_C(t). \tag{2.16}$$

Substituting equation 2.16 into 2.14 the following expression is obtained

$$\begin{cases} V_a(t) = \frac{2}{3}V_A(t) - \frac{1}{3}(V_B(t) + V_C(t)) \\ V_b(t) = \frac{2}{3}V_B(t) - \frac{1}{3}(V_A(t) + V_C(t)) \\ V_c(t) = \frac{2}{3}V_C(t) - \frac{1}{3}(V_B(t) + V_A(t)) \end{cases} \tag{2.17}$$

The phase voltage can also be expressed as a function of switch position from equation 2.13 and 2.17

$$\begin{cases} V_a(t) = \frac{V_{DC}}{3}(2S_{A_h} - S_{B_h} - S_{C_h}) \\ V_b(t) = \frac{V_{DC}}{3}(2S_{B_h} - S_{A_h} - S_{C_h}) \\ V_c(t) = \frac{V_{DC}}{3}(2S_{C_h} - S_{B_h} - S_{A_h}) \end{cases} . \tag{2.18}$$

The resulting phase and line voltages for all possible switch positions can be seen in table 2.2 on page 22.

2.4.2 MOSFET or IGBT

Up to the 1970s and the introduction of the Metal Oxide Semiconductor Field Effect Transistor (MOSFET) the only power transistor was the Bipolar Junction Transistor (BJT). The BJT is a current controlled transistor, meaning it always has to flow a current through the base to emitter circuit for it to conduct. It also has a relatively slow turn off characteristics and is prone to thermal runaway due to its negative temperature coefficient.

High power BJT also have a low current amplification factor h_{FE} around 5-10 times, thus needed to be coupled in a Darlington configuration to get high output currents.[14][15]

The MOSFET is a voltage controlled transistor where the voltage between gate and source control the current from drain to source, no current flows through from the gate to source. The MOSFET is capable of very fast switching, from a few tens to a few hundred nanoseconds. The MOSFET has a positive thermal coefficient, thus resistance will increase with the temperature making it less prone to thermal runaway. The conducting resistance r_{DSon} is heavily depending on the blocking voltage rating VB_{DSS} according to

$$r_{DSon} = kVB_{DSS}^{2.5-2.7}. \tag{2.19}$$

Where k is a constant depending on the transistors geometry. The MOSFETs are therefore only available with low r_{DSon} for low voltage devices and are therefore available in either medium voltage and low current or low voltage and high current.[14][15]

In the 1980s the Insulated Gate Bipolar Transistor (IGBT) was introduced, it can be seen as a combination between the BJT and the MOSFET. It shares the BJT conduction and switching characteristics and the voltage control from the MOSFET. Just like the BJT the IGBT has a close to constant voltage loss over the device, thus the voltage drop is not depending on the voltage rating as the MOSFET. This makes it possible to manufacture IGBTs with both high voltage and current ratings.[14][15]

An estimation about how to choose between the types of high power switches can be seen in figure 2.7, the limitations however should be seen as a guidance not a hard limit. Choosing the right device would probably be a tradeoff between different parameter in the inverter design, especially close to the limitations. The devices are also constantly evolving and their limits are moved.

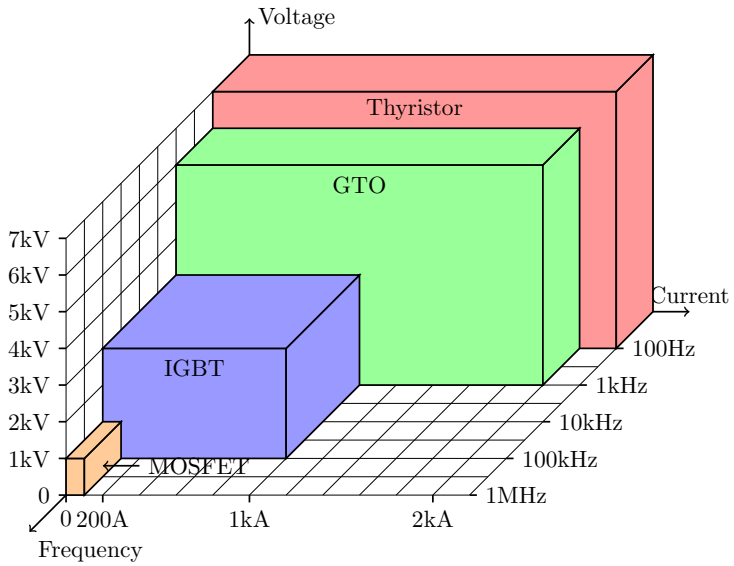

Figure 2.7: Typical ratings for different high power semiconductors.

2.4.3 Gate Drivers

Gate drivers are used for switching the semiconductor device between the on and off states. They are designed to supply a high gate current to charge and discharge the gate capacitance to minimize the switching time, thus minimizing the time spent traversing

the active region and the switching losses associated with the region. Fast switching can however have drawbacks such as high voltage spikes at turn off.

Gate Charge

The IGBT switching characteristics is determined by the internal capacitances and the external resistances. As seen in figure 2.8 there are three major capacitances to consider, the Gate-Emitter C_{GE}, Gate-Collector C_{GC} and Collector-Emitter C_{CE}.[16] Figure 2.9b

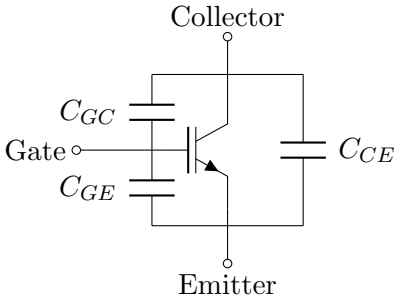

Figure 2.8: IGBT and its internal capacitances.

shows the Gate-Emitter voltage, Collector-Emitter voltage, Gate current and Collector current as a function of time. The turn on process can be described in the four steps shown in the figure.

- t0-t1: the gate voltage is turned on at t0 and the Gate-Emitter capacitance will charge until threshold voltage $V_{GE(th)}$ where the IGBT starts to conduct.
- t1-t2: the Gate-Emitter voltage keeps rising until it reaches the Miller plateau voltage $V_{GE(pl)}$.
- t2-t3: the Gate-Emitter voltage is constant while the Gate-Collector capacitance is charging.
- t3-t4: The IGBT is now fully turned on, but the Gate-Emitter capacitance keeps charging until the saturation voltage $V_{GE(on)}$ is reached.

The turn off will happen in the opposite order.

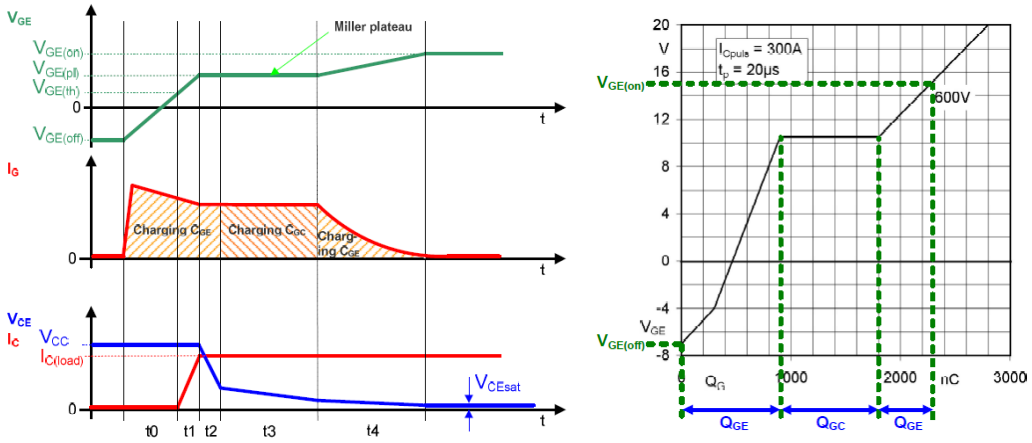

(a) Simplified gate charge waveforms. (b) Gate charge characteristics.

Figure 2.9: Gate charging of a IGBT.[4]

Figure 2.9 shows the Gate-Emitter voltage as a function of total Gate charge. The majority of the switching losses occur between t2 and t3 where the Gate-Emitter voltage is constant at a level where the IGBT is in its active region with a large voltage drop across the Collector and Emitter.

Gate Resistors

The gate resistor affect the switching time, switching losses, reverse bias safe operating area, short circuit safe operating area, electromagnetic interference, $\frac{dv}{dt}$, $\frac{di}{dt}$ and reverse recovery current of the freewheeling diode[17] by limiting the charge and discharge current (figure 2.10) into the IGBT's gate, thus limiting the rise and fall time of the gate capacitance charge. The selection of the gate resistors has to be done with consideration

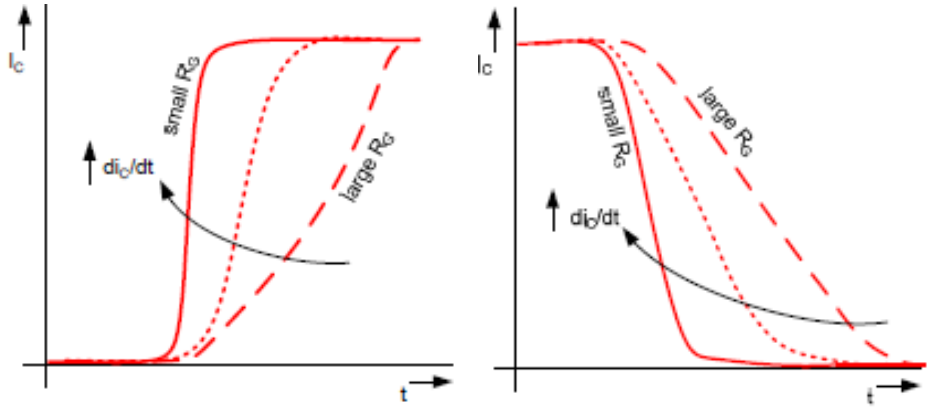

(a) di_c/dt turn on. (b) di_c/dt turn off.

Figure 2.10: Rise- and fall-time vs gate resistance.[5]

of the whole inverter design, e.g. IGBT type, freewheeling diode, switching frequency, losses, layout, stray inductance, DC-link voltage and driver capacity. A driver normally uses separate on R_{gon} and off R_{goff} resistor to be able to tune the turn on and turn off

[4]IGBT Driver Calculation, Semikron
[5]Gate Resistor - Principles and Applications, Semikron

characteristics separately, see figure 2.11. The typical turn on volgate V_{gon} is $+15V$ and turn off voltage V_{goff} is between $-5V$ to $-15V$.

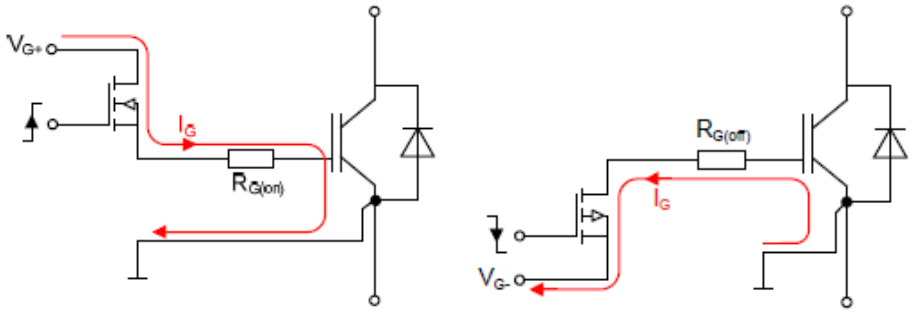

(a) Turn on gate current path. (b) Turn off gate current path.

Figure 2.11: Turn on and off current paths.[6]

2.5 LabVIEW

Laboratory Virtual Instrumentation Engineering Workbench (LabVIEW) is a system design and development platform used for data acquisition, instrument control and industrial automation. The main programming language is "G", a graphical programming language where different functions are connected together with virtual wires. The function blocks are called VI and the basic functions are integrated with LabVIEW environment, more advanced function can be bought as add on modules or created by the user. The execution order of the program is dependent on the program structure each VI executes sequentially when input data is available to all inputs. But the program can also be divided into branches that executes in parallel. The programming interface is closely tied to a Human

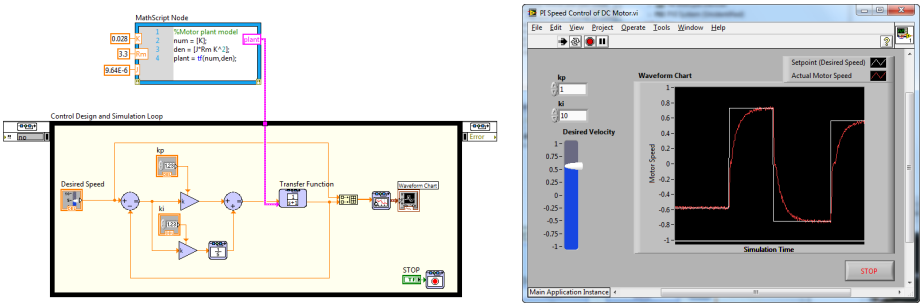

(a) G code. (b) User interface.

Figure 2.12: Example of LabVIEW G code and user interface.[7]

Machine Interface (HMI) window where the VI's such as indicators, input values/buttons, graphic plots, etc. shows up to provide control and visualization of the process parameters. Figure 2.12 shows a example of a PID regulator implemented in LabVIEW.

[6] Gate Resistor - Principles and Applications, Semikron
[7] `http://www.ni.com/white-paper/12944/en`

2.6 CompactRIO

The CompactRIO is a multipurpose control system manufactured by National Instruments, it contains a real time controller with a Real Time Operating System (RTOS), a Field Programmable Gate Array (FPGA) and a selection of Reconfigurable Input Output modules. The RIO also provides Ethernet and Serial communication for programming the device and to transfer data to, from and between other RIOs and desktop computers.

Figure 2.13: CompactRIO controller with 8 IO-modules.[8]

2.6.1 Real Time Operating System

A RTOS is designed for timing rather than computational speed to be able to make the system behave in a more deterministic way. This is achieved by focusing on minimal interrupt latency and minimal thread switching latency to make sure that all tasks runs in its specified time. A RTOS should be able to:

- Perform tasks within a guaranteed worst-case time frame.
- Carefully prioritize different sections of your program.
- Run loops with nearly the same timing on each iteration.
- Detect if a loop missed its timing goal.

2.6.2 Field Programmable Gate Array

The FPGA is the heart of the RIO control system, it provides reconfigurable connections between the IO-modules, and communication interfaces. This direct connection is a big speed advantage compared to systems that uses a data bus connection between the IO-module. The other big advantage with the FPGA is that it also can be configured to perform high speed calculations.

2.6.3 IO-Modules

National Instruments offer a wide range of different module types, such as:

[8] `http://www.keisoku-gb.com/new/photo/07Dec/NI_compactRIO.jpg`

- Digital input/output
- Analog input/output
- Current measurement
- Counters/Pulse generators
- Thermocouple modules
- Communication modules

2.7 MCU/DSP

An alternative to the CompactRIO and LabVIEW is to use a Micro Controller Unit (MCU) or a Digital Signal Processor (DSP). They are available from most of the large semiconductor manufacturers in a wide variety of performance, functionality and pin-out choices for all kind of applications. The main advantage over the CompactRIO is price, but there are also drawbacks. As seen in figure 2.14a they are sold without any

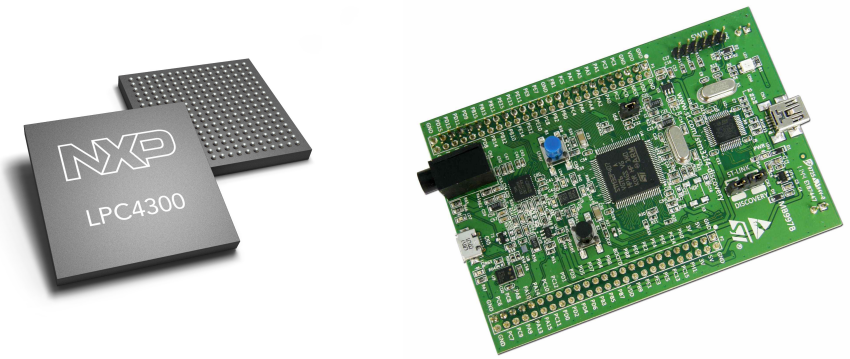

(a) NXP ARM Cortex-M4 (b) STM32F4 Discovery development board

Figure 2.14: Micro controllers.[9]

peripheral equipment. A step to a more useful solution is a development board. Figure 2.14b shows a development board from STMicroelectronics, it is equipped with a 168MHz ARM processor, programming/debugging interface, pin headers for I/O, etc. But there is still a need for more peripheral electronics to adapt the signal levels for measurement and control signals. The most cost effective solution for commercial inverter production would probably be a complete custom control board with either a MCU/DSP or a FPGA.

The programming of the MCU is normally done in the language "C" or assembly which unlike LabVIEW is a text based language that probably is harder to get started with for an inexperienced user. If a HMI is needed it also has to be created as separate application.

For a HMI there is no natural connection between the code and the HMI like in LabVIEW, it has to be created as a separate application with a suitable communication protocol between the MCU and host computer.

[9](a) - http://www.nxp.com/scale-image/w-240/wcm_documents/news/press-releases/2011/LPC4300.jpg (b) - http://blog.tkjelectronics.dk/wp-content/uploads/STM32F4-DISCOVERY_Board.jpg

2.8 Control Theory

To be able to run synchronous motors with variable speed a Variable Frequency Drive (VFD) has to be used. A VFD is basically like the inverter described in chapter 2.4 together with a switching and control unit that controls the inverter switches to achieve the requested torque, speed, position, etc. Two main control approaches exist, Scalar- or Vector- control.[3]

Scalar control controls only the magnitude of the inverter output, i.e. frequency and voltage or current. The control algorithm aims to keep the ratio between for example voltage and frequency constant, giving the control its name V/f-control. The method is an open loop approach that doesn't need any position or motor current feedback. The lack of feedback results in a drive with poor dynamic performance, the method is therefore mostly used for low performance applications such as fans and pump drives.[18] However, for induction motors the method is widely adopted.

2.8.1 Vector Control

A method to increase the dynamic performance is to use a control method with current, voltage and position feedback, such as Vector Control instead of scalar control. Vector Control aims at controlling the angle and magnitude of the flux linkage vector. There are two different strategies for implementing vector control, Field Oriented Control (FOC) and Direct Torque Control (DTC). To simplify the calculations both of them are implemented by transforming the normal three phase reference frame into a two phase reference frame by using the Park and Clarke transforms.[3]

2.8.2 Clarke and Park Transformations

The Clarke and Park transformations are done to simplify calculations on electric machines by transforming variables in the normal three-phase reference frame to an orthogonal reference frame, these new reference frames can be either stationary (Clarke) like the original rotor reference frame or rotating with the rotor (Park). A illustration of the different reference frames is shown in figure 2.15.

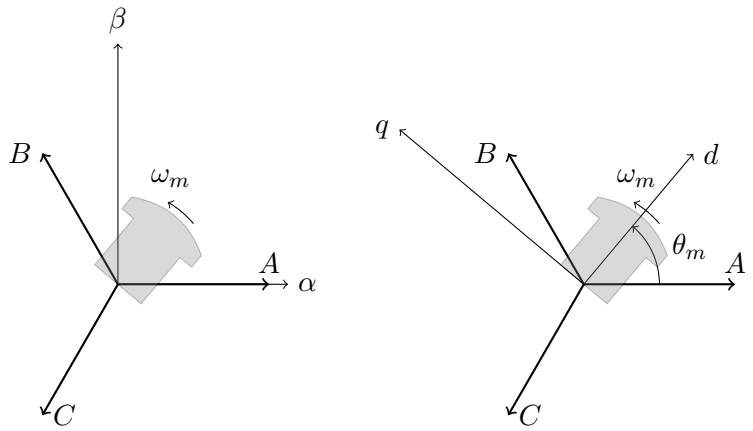

(a) ABC to $\alpha\beta 0$ (b) ABC to $qd0$

Figure 2.15: Clarke and Park transform.

Clarke

The Clarke transform was developed by E. Clarke[19] to transform a three-phase stationary reference frame into a two-phase orthogonal reference frame, the new two-phase variables are denoted α and β. Equation 2.20 shows the transformation from abc to $\alpha\beta 0$, where f can represent the voltage, current, flux linkages or electric charge

$$[f_{\alpha\beta 0}] = T_{\alpha\beta 0}\,[f_{abc}] \tag{2.20}$$

where

$$f_{\alpha\beta 0} = [f_\alpha \quad f_\beta \quad f_0]^T \tag{2.21}$$

and

$$f_{abc} = [f_a \quad f_b \quad f_c]^T \tag{2.22}$$

and the transformation matrix $T_{\alpha\beta 0}$ is

$$T_{\alpha\beta 0} = \frac{2}{3}\begin{bmatrix} 1 & -\frac{1}{2} & -\frac{1}{2} \\ 0 & \frac{\sqrt{3}}{2} & -\frac{\sqrt{3}}{2} \\ \frac{1}{2} & \frac{1}{2} & \frac{1}{2} \end{bmatrix}. \tag{2.23}$$

The inverse transformation is given by equation 2.24

$$f_{abc} = T^{-1}_{\alpha\beta 0}\,[f_{\alpha\beta 0}] \tag{2.24}$$

and the inverse transformation matrix $T^{-1}_{\alpha\beta 0}$ is

$$T^{-1}_{\alpha\beta 0} = \begin{bmatrix} 1 & 0 & 1 \\ -\frac{1}{2} & \frac{\sqrt{3}}{2} & 1 \\ -\frac{1}{2} & -\frac{\sqrt{3}}{2} & 1 \end{bmatrix}. \tag{2.25}$$

Park

The Park transform was developed by R. H. Park[20] as a revolutionary method for analysis of electric machines. The approach is to transform the stator parameters into a reference frame that rotates with the rotor, by doing this all parameters can be seen as constant values. The new two-phase variables are denoted d and q for direct- and quadrature-axis. This greatly simplifies machine calculations since the time varying inductance parameters in the voltage equations are eliminated. Equation 2.26 shows the transformation from abc to $qd0$, where f can represent the voltage, current, flux linkages or electric charge

$$[f_{qd0}] = T_{qd0}(\theta)\,[f_{abc}] \tag{2.26}$$

where

$$f_{qd0} = [f_q \quad f_d \quad f_0]^T \tag{2.27}$$

and

$$f_{abc} = [f_a \quad f_b \quad f_c]^T \tag{2.28}$$

and the transformation matrix T_{qd0} is

$$T_{qd0} = \frac{2}{3}\begin{bmatrix} cos(\theta) & cos(\theta - \frac{2\pi}{3}) & cos(\theta + \frac{2\pi}{3}) \\ sin(\theta) & sin(\theta - \frac{2\pi}{3}) & sin(\theta + \frac{2\pi}{3}) \\ \frac{1}{2} & \frac{1}{2} & \frac{1}{2} \end{bmatrix}. \tag{2.29}$$

The inverse transformation is given by equation 2.30

$$f_{abc} = T_{qd0}^{-1}(\theta)\,[f_{qd0}] \tag{2.30}$$

and the inverse transformation matrix T_{qd0}^{-1} is

$$T_{qd0}^{-1}(\theta) = \begin{bmatrix} cos(\theta) & sin(\theta) & 1 \\ cos(\theta - \frac{2\pi}{3}) & sin(\theta - \frac{2\pi}{3}) & 1 \\ cos(\theta + \frac{2\pi}{3}) & sin(\theta + \frac{2\pi}{3}) & 1 \end{bmatrix}. \tag{2.31}$$

Field Oriented Control

With Field Oriented Control the main goal is to control the drive in such way that it produces a Maximum Torque Per Ampere (MTPA) as it will give the highest efficiency. This is achieved by independently controlling the direct- and quadrature- axis currents according to their optimal values for any given torque. The optimal currents are depending of the machines electromagnetic properties.

Maximum Torque Per Ampere for Positive Saliency

There is a number of different ways to calculate the MTPA current trajectory[3]. The one used in this thesis is based on the work of T. M. Jahns[21] with changes by A. Kronberg[3] to adapt it for use with a motor with positive saliency. Figure 2.16 shows the current trajectory as a function of torque. The blue curves represent the torque from 0.25 to 1.25, placing the current vector on any point of one of these curves will result in the same torque but a different current magnitude. The red curve represents the MTPA current trajectory, which is the shortest possible current vector for any torque value.

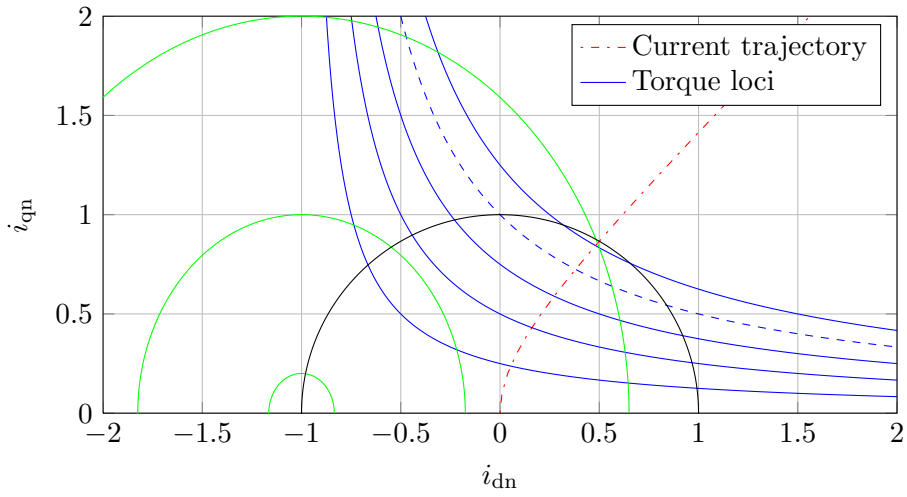

Figure 2.16: Constant torque loci and current trajectory for MTPA.

Figure 2.17 shows the individual direct- and quadrature- axis currents as a function of torque.

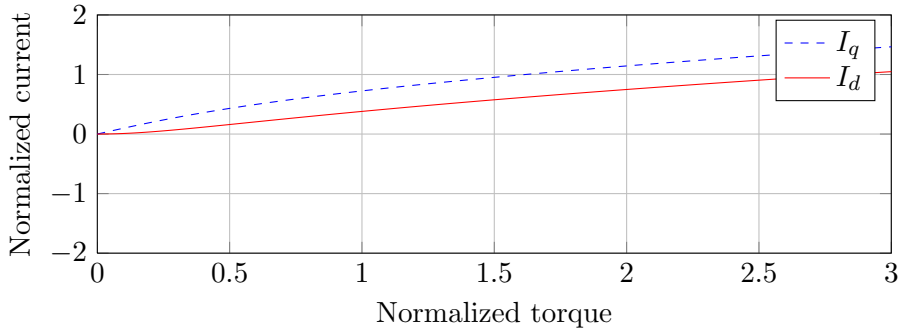

Figure 2.17: Direct- and quadrature-axis currents reference.

The torque produced for salient pole motor can be described by

$$T_e = \frac{3}{2}\frac{p}{2}\left[\lambda_{pm} i_q - (L_q - L_d) i_d i_q\right] \tag{2.32}$$

where
λ_{pm} is the flux linkage per phase from the excitation system.
I_q and I_d is the quadrature- and direct- axis currents.
L_q and L_d is the quadrature- and direct- axis inductances.
By following the steps of normalization, derivation and equation solving[3] we get a expression for normalized current as a function of normalized torque

$$i_{qn} = \frac{1}{2}\sqrt{A + B - C} - \frac{1}{2}\sqrt{D} \tag{2.33}$$

and

$$i_{dn} = \frac{T_{en}}{i_{qn}} - 1 \tag{2.34}$$

where

$$A = \frac{4\sqrt[3]{\frac{2}{3}}T_{en}^2}{\sqrt[3]{9T_{en}^2 + \sqrt{3}\sqrt{256T_{en}^6 + 27T_{en}^4}}}$$

$$B = \frac{2T_{en}}{\sqrt{\frac{\sqrt[3]{9T_{en}^2+\sqrt{3}\sqrt{256T_{en}^6+27T_{en}^4}}}{\sqrt[3]{23}^{\frac{2}{3}}} - \frac{4\sqrt[3]{\frac{2}{3}}T_{en}^2}{\sqrt[3]{9T_{en}^2+\sqrt{3}\sqrt{256T_{en}^6+27T_{en}^4}}}}}$$

$$C = \frac{\sqrt[3]{9T_{en}^2 + \sqrt{3}\sqrt{256T_{en}^6 + 27T_{en}^4}}}{\sqrt[3]{23}^{\frac{2}{3}}}$$

$$D = \frac{\sqrt[3]{9T_{en}^2 + \sqrt{3}\sqrt{256T_{en}^6 + 27T_{en}^4}}}{\sqrt[3]{23}^{\frac{2}{3}}} - \frac{4\sqrt[3]{\frac{2}{3}}T_{en}^2}{\sqrt[3]{9T_{en}^2 + \sqrt{3}\sqrt{256T_{en}^6 + 27T_{en}^4}}}.$$

The equation for the quadrature axis current is quite complex and can be too hard for a control system to calculate in real time. But with the use of normalized values it is possible to pre calculate the values and store them in a lookup table. When changing the motor the only thing needed to be changed in the control system is the base values.

2.8.3 Sinusoidal Pulse Width Modulation

Sinusoidal Pulse Width Modulation (SPWM) is a very common PWM scheme. A high frequency triangular carrier wave is compared to the sinusoidal modulating wave with the desired frequency and amplitude. Figure 2.18 shows the modulation signal and a low frequency carrier wave, a higher frequency gives a smother voltage but higher switching losses. If the modulation wave amplitude gets higher than the carrier the output is turned

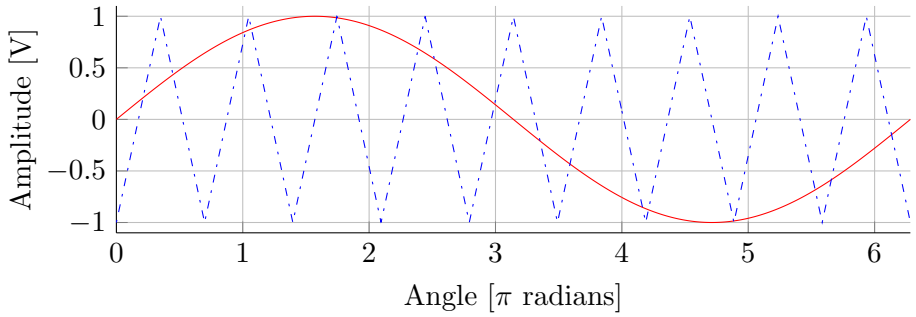

Figure 2.18: Sinusoidal modulation and triangular carrier wave.

on, if the modulation wave amplitude falls below the carrier the output is turned off. Figure 2.19 shows the resulting variable pulse width square wave switching pattern and a ideal low pass filtered sinusoidal version.

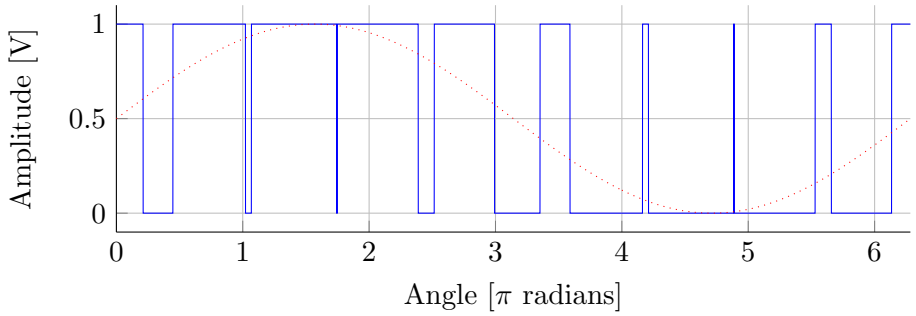

Figure 2.19: SPWM switching pattern.

2.8.4 Space Vector Modulation

Space Vector Modulation (SVM) can be done with the same modulation technique as SPWM. The difference is that the modulation signal is shaped to allow a higher utilization of the DC-link voltage. Another way to reach a higher utilization of the DC-link voltage is to superimpose a 3rd harmonic with 1/6th of the fundamental amplitude, both methods gives a 15.4% higher utilization.

For a three phase two level inverter there is 2^3 possible switching states, each giving eight different sets of phase- and line-to-line output voltage. The different output voltages can be seen in table 2.2, where V_{DC} is the DC-link voltage.[13]

Table 2.2: Possible switch positions with their resulting phase and line to line voltages for a three phase inverter.

a	b	c	V_{an}	V_{bn}	V_{cn}	V_{ab}	V_{bc}	V_{ca}
0	0	0	0	0	0	0	0	0
0	0	1	$\frac{-V_{DC}}{3}$	$\frac{-V_{DC}}{3}$	$\frac{2V_{DC}}{3}$	0	$-V_{DC}$	V_{DC}
0	1	0	$\frac{-V_{DC}}{3}$	$\frac{2V_{DC}}{3}$	$\frac{-V_{DC}}{3}$	$-V_{DC}$	V_{DC}	0
0	1	1	$\frac{-2V_{DC}}{3}$	$\frac{V_{DC}}{3}$	$\frac{V_{DC}}{3}$	$-V_{DC}$	0	V_{DC}
1	0	0	$\frac{2V_{DC}}{3}$	$\frac{-V_{DC}}{3}$	$\frac{-V_{DC}}{3}$	V_{DC}	0	$-V_{DC}$
1	0	1	$\frac{V_{DC}}{3}$	$\frac{-2V_{DC}}{3}$	$\frac{V_{DC}}{3}$	V_{DC}	$-V_{DC}$	0
1	1	0	$\frac{V_{DC}}{3}$	$\frac{V_{DC}}{3}$	$\frac{-2V_{DC}}{3}$	0	V_{DC}	$-V_{DC}$
1	1	1	0	0	0	0	0	0

From equation 2.20 and table 2.2 it is possible to calculate the Clarke transformed two phase quantities U_α and U_β and the resulting voltage vector U_{xxx} for each switching state. For a balanced system the equation can be simplified to equation 2.35 and the calculated voltage states can be seen in table 2.3. U_{000} and U_{111} is called zero vectors, a state where there is no output voltage from the inverter.

$$\begin{cases} V_\alpha = V_{AN} \\ V_\beta = \frac{V_{AN}+2V_{BN}}{\sqrt{3}} \end{cases} \tag{2.35}$$

Table 2.3: Possible switch positions with their transformed $\alpha\beta$ voltages for a three phase inverter.

a	b	c	V_α	V_β	Vector
0	0	0	0	0	0_{000}
0	0	1	$-\frac{V_{DC}}{3}$	$-\frac{V_{DC}}{3}$	U_{240}
0	1	0	$\frac{V_{DC}}{3}$	$\frac{V_{DC}}{3}$	U_{120}
0	1	1	$-\frac{2V_{DC}}{3}$	0	U_{180}
1	0	0	$\frac{2V_{DC}}{3}$	0	U_0
1	0	1	$\frac{V_{DC}}{3}$	$-\frac{V_{DC}}{3}$	U_{300}
1	1	0	$\frac{V_{DC}}{3}$	$\frac{V_{DC}}{3}$	U_{60}
1	1	1	0	0	0_{111}

The goal of Space Vector Modulation is to synthesize a output voltage vector U_{out} by using the eight possible switching states. When using Space Vector Modulation the control algorithm divides one electrical revolution of the machine into six sectors spanning 60 degrees enclosed by one voltage vector U_{xxx} on each side. In each sector there is only four valid switching states, the two active vectors adjacent to the sector and the two zero vectors. By calculating the time for each switching state any output voltage vector can be synthesized, from $0 - 360°$ and from $0 - \frac{2}{3}V_{DC}$.

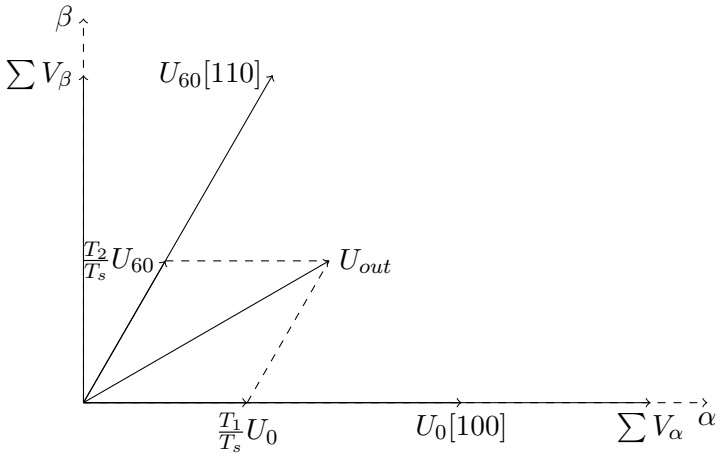

Figure 2.20: Space vector modulation geometry.

The output vector U_{out} for the sector between 0° and 60° seen in figure 2.20 can be described by equation 2.36

$$\begin{cases} T_s = T_1 + T_2 + T_0 \\ U_{out} = \frac{T_1}{T_s}U_0 + \frac{T_2}{T_s}U_{60} \end{cases} \tag{2.36}$$

where T_1, T_2 and T_0 is extent of time spent with the vectors 0_0, 0_{60} and zero vector applied, T_s is the period time of the PWM switching frequency. The projected vectors U_α and U_β of U_{out} can be calculated from equation 2.37

$$\begin{cases} U_\alpha = \frac{T_1}{T_s}|U_0|cos(0) + \frac{T_2}{T_s}|U_{60}|cos(60) \\ U_\beta = 0 + \frac{T_2}{T_s}|U_{60}|sin(60) \end{cases} . \tag{2.37}$$

Normalizing the space vector magnitude $\frac{2V_{dc}}{3}$ with respect to maximum phase voltage $\frac{V_{dc}}{\sqrt{3}}$ gives a normalized space vector magnitude of $\frac{2}{\sqrt{3}}$. Inserting in 2.37 and solving for T_1 and T_2 gives equation 2.38.

$$\begin{cases} T_1 = \frac{T_s}{2}(\sqrt{3}U_\alpha - U_\beta) \\ T_2 = T_s U_\beta \end{cases} \tag{2.38}$$

Where for T_1 and T_2 are the time spent with active vectors applied as a function of normalized U_α and U_β voltage, the rest of the period T_0 is spent with one of the zero vectors applied. The duty cycle t_1 and t_2 for the active vectors are calculated from equation 2.40.

$$T_0 = T_s - T_1 - T_2 \tag{2.39}$$

$$\begin{cases} t_1 = \frac{T_1}{T_s} = \frac{1}{2}(\sqrt{3}U_\alpha - U_\beta) \\ t_2 = \frac{T_2}{T_s} = U_\beta \end{cases} \tag{2.40}$$

If the same calculations are applied for the sector between 60° and 120° equation 2.41 is obtained.

$$\begin{cases} t_1 = \frac{T_1}{T_s} = \frac{1}{2}(-\sqrt{3}U_\alpha + U_\beta) \\ t_2 = \frac{T_2}{T_s} = \frac{1}{2}(\sqrt{3}U_\alpha + U_\beta) \end{cases} \tag{2.41}$$

Repeating the calculations for all sectors shows there are six possible values that can be defined as

$$\begin{cases} X = U_\beta \\ Y = \frac{1}{2}(\sqrt{3}U_\alpha + U_\beta) \\ Z = \frac{1}{2}(-\sqrt{3}U_\alpha + U_\beta) \end{cases} \tag{2.42}$$

and $-X$, $-Y$ and $-Z$. The duty cycles for the active vectors in all sectors can be seen in table 2.4.

Table 2.4: Definition of t1 and t2 in the six sectors.

Sector	0-60°	60-120°	120-180°	180-240°	240-300°	300-0°
t1	-Z	Z	X	-X	-Y	Y
t2	X	Y	Y	Z	-Z	-X

By using a modified Clarke transform the sector can be determined by a simple comparison of the calculated reference voltage.

$$\begin{cases} V_{ref1} = U_\beta \\ V_{ref2} = \frac{1}{2}(-U_\beta + \sqrt{3}U_\alpha) \\ V_{ref3} = \frac{1}{2}(-U_\beta - \sqrt{3}U_\alpha) \end{cases} \tag{2.43}$$

Equation 2.43 gives a three phase voltage that is 90° advanced compared to the normal inverse Clarke transform. By comparing this voltage with zero

$$\begin{cases} V_{ref1} \leqslant 0, & a = 0 \\ V_{ref2} \leqslant 0, & b = 0 \\ V_{ref3} \leqslant 0, & c = 0 \end{cases} \quad \begin{cases} V_{ref1} > 0, & a = 1 \\ V_{ref2} > 0, & b = 1 \\ V_{ref3} > 0, & c = 1 \end{cases} \tag{2.44}$$

it is the possible to determine the sector from the binary value of a, b and c. The relationship between the binary sector number N_{bin} and the real sector number S can be seen in table 2.5

$$N_{bin} = 4c + 2b + a \tag{2.45}$$

Table 2.5: Real sector number vs binary sector number.

N_{bin}	3	1	5	4	6	2
S	1	2	3	4	5	6

One of the goals with SVM is to only change the state of one switch at the time, the turn on time for the first sector is therefore defined as

$$\begin{cases} t_{aon} = \frac{T_s - t_1 - t_2}{2} \\ t_{bon} = t_{aon} + t_1 \\ t_{con} = t_{aon} + t_2. \end{cases} \tag{2.46}$$

The turn on time is then assigned to the other sectors according to table 2.6

Table 2.6: Duty cycle assignment.

Sector	0-60°	60-120°	120-180°	180-240°	240-300°	300-0°
T_a	t_{aon}	t_{bon}	t_{con}	t_{con}	t_{bon}	t_{aon}
T_b	t_{bon}	t_{aon}	t_{aon}	t_{bon}	t_{con}	t_{con}
T_c	t_{con}	t_{con}	t_{bon}	t_{aon}	t_{aon}	t_{bon}

which will give the following switching pattern where only one switch at the time changes state.

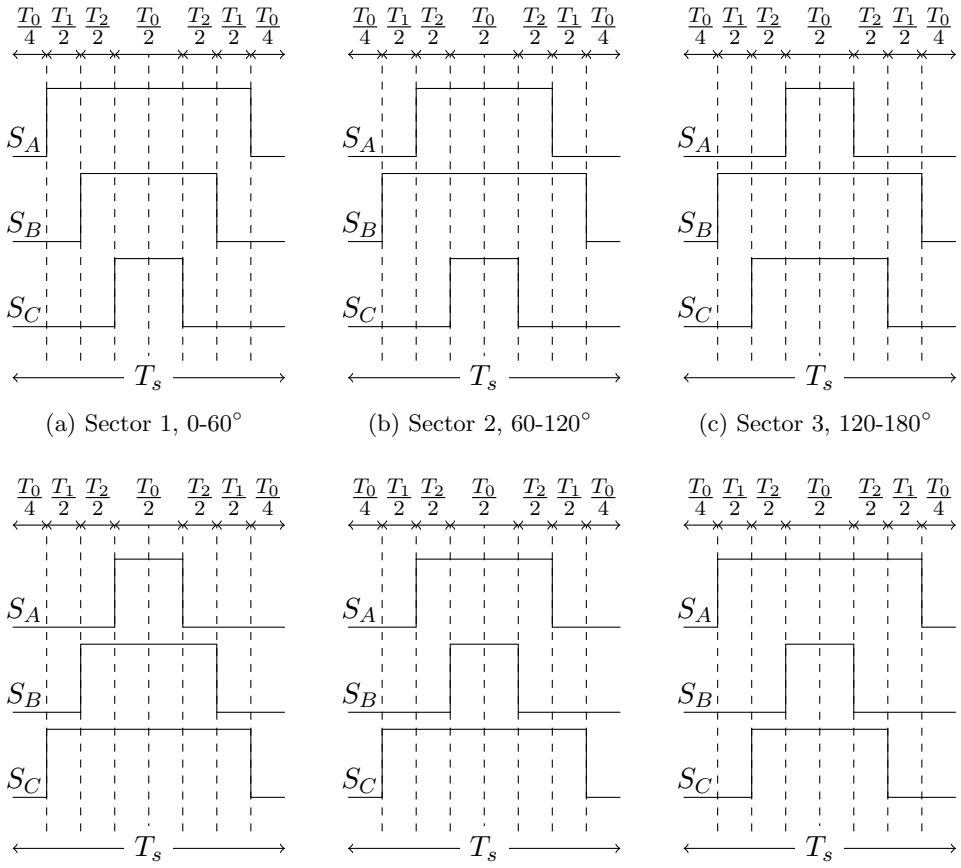

(a) Sector 1, 0-60° (b) Sector 2, 60-120° (c) Sector 3, 120-180°

(d) Sector 4, 180-240° (e) Sector 5, 240-300° (f) Sector 6, 300-0°

Figure 2.21: Switching pattern for space vector modulation in all six sectors.

The resulting duty cycles for the three phases can be seen in figure 2.22 Modulating the duty cycle waveform with a high frequency triangular wave like in SPWM, will give a phase voltage with the same waveform as the duty cycle.[13][22]

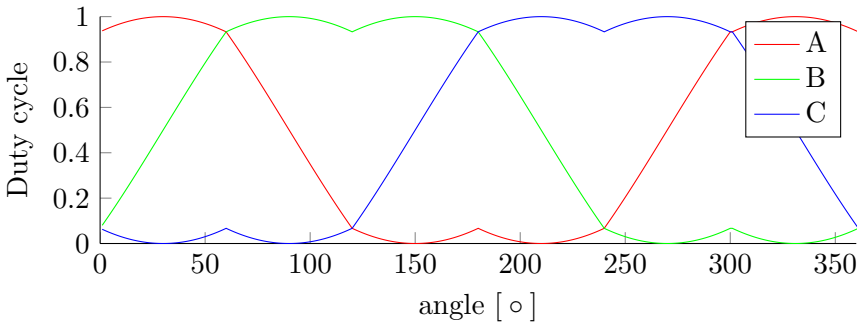

Figure 2.22: SVM PWM modulation waveform.

Chapter 3

Hardware Implementation

3.1 Introduction

The implementation of the inverter was performed in three different stages. The first step was to determine the needed input/outputs etc. for the control system, and putting the system together, whereas the second step was to construct a cheap small scale inverter to test the control systems hardware and software design. The third step was to construct the large scale inverter that is the main purpose of this project.

3.2 Control System

For a rapid prototype development the FPGA based CompactRIO together with its graphical programming language software LabVIEW from National Instruments was chosen. The software also offers an easy way to control the motor via a Human Machine Interface (HMI). The use of a MCU would make the system harder to debug and need additional software programming for a communication and control interface, it will also need design and construction of additional hardware between MCU and the inverters electronics.

The minimum Input/Outputs needed for the system is:

- 6x Digital outputs for gate driving
- 3x Digital inputs for position sensor
- 2x Analog inputs for current measurement

The CompactRIO and LabVIEW equipment used are:

- 1x CompactRIO 9074 Chassis
- 2x CompactRIO 9401 Digital I/O
- 1x CompactRIO 9221 Analog In
- 1x CompactRIO PSU
- 1x LabVIEW 2011 Professional Development System Software
- 1x LabVIEW 2011 FPGA Development Software
- 1x LabVIEW 2011 SP1 SoftMotion Premium Software
- 1x Computer

3.3 Small Scale Inverter

3.3.1 Introduction

To be able to test the control system rapidly a small scale inverter was constructed of leftover parts from other projects. The parts used are:

- 6x IXYS IXFN140N20P MOSFET.
- 1x IRF IR2130 MOSFET driver with external components.
- 1x Heat sink
- 1x Robbe Roxxy BL2815 70W brushless DC motor.
- 1x Leine & Linde incremental encoder.
- 2x LEM HAL-50S current transducer.
- 1x Prototype board.
- Wires, Connectors, Couplings, Lego, etc.
- CompactRIO with digital in-/output and analog input modules.

3.3.2 Setup

The MOSFETs were mounted on the heat sink and connected in a tree legged bridge configuration, see figure 3.1a. The driver cards gate drive outputs and their grounds where connected to each MOSFET between gate and emitter, the inputs to the driver card were directly connected to digital output module of the CompactRIO and the encoder was connected to a digital input module. One motor phase wire was connected to each leg of the inverter and the motor and inverter shafts were then connected to each other with a shaft coupling, the two parts were then align and mounted together with Lego and rubber bands (figure 3.1b).

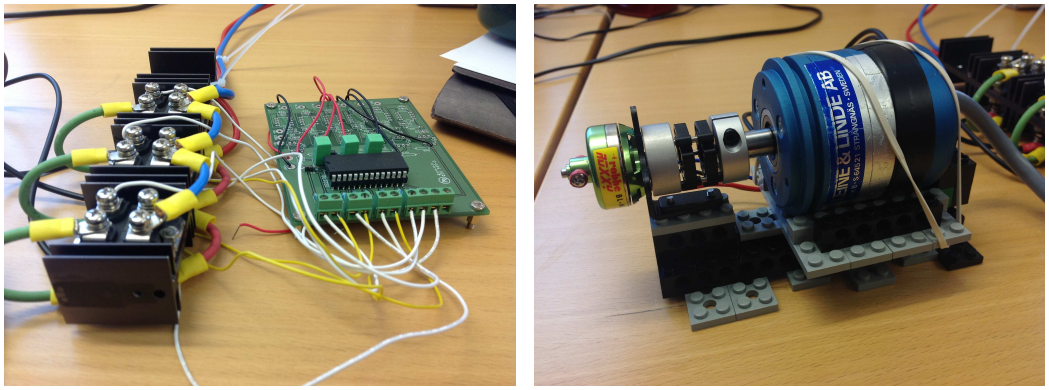

(a) Three legged inverter bridge. (b) Motor and encoder

Figure 3.1: Small scale inverter set up.

3.4 Full Size Inverter

3.4.1 Introduction

The main goal of this project is to construct an inverter for use with our 30kW motor, briefly described in chapter 2.2.4.

3.4.2 Component Selection

To make the inverter work properly it's important to choose the right components. Previously constructions of high power high voltage electronics at the university have successfully used Semikrons IGBTs as power switches, so a decision was made to continue on this track. As a help to choose the correct IGBTs and cooling, Semikrons SEMISEL software was used. Some values were changed from default but most were left untouched, the topology was chosen as a three phase DC to AC converter and the DC voltage was set to $330V$ to get the motors rated voltage on the AC output. The output power was set to $30kW$ and the overload factor to 1.5 times rated power for 10s. The overload factor was lowered from the default value of 2.0 to be able to use a SEMITRANS 2 module and still pass the temperature criteria. The use of this module made it possible use the P3 heat sink and its kit with mounting rails and bus bars, thus reducing the construction time when no drilling and tapping of the heat sink and bus bars is needed.

IGBT

The IGBT chosen is the largest SEMITRANS 2 module available, it's rated for $600V_{CE}$ and $150A$ at $80°C$ and has a typical turn on time T_{don} of $150ns$ and a turn off time T_{doff} of $490ns$. The gate charge Q_G is an important parameter when choosing the driver, the SKM 145GB066D used in this project needs a minimum of $1100nC$ to fully conduct.

Driver

The driver chosen is the SKYPER 32PRO R together with the generic adaptor board BOARD 1 SKYPER 32PRO R, there is also more specialized adapter board available to mount the driver directly on top of the SEMiX and SKiM modules. This driver has previously been tried at the university without succeeding to get it to work, so let's go for that one. The driver and board together are rated for voltages up to $1700V_{CE}$ and can deliver a gate charge of $6300nC$.

Current Measuring

As current measurement sensor a hall effect type sensor was chosen, the LEM HAL 50-S is rated for $50A_{RMS}$ and $\pm 150A$ peak current. The sensor provides isolation from the phase voltage and is equipped with potentiometers for gain and offset adjustments.

Position Measuring

As position sensor an incremental encoder was chosen, the Hengstler RI 80-E with a 45mm hollow shaft and 2048 pulses per revolution. The tree hall effect sensor method was ruled out because of the inaccuracy in the method. Other sensor types need to be mounted at the shaft end of the motor, thus increasing the total length. They also need fabrication of fastening brackets, shaft coupling, etc. With a hollow shaft the encoder can be mounted directly on the shaft between the rotor and shaft bearing support, not increasing the

machine length. The intention was to use an encoder with around 1000ppr to get a resolution of 0.09° with X4 encoding, but finding someone that can deliver a 45mm hollow shaft encoder in a reasonable time was hard. One company had a discontinued model in stock with 2048ppr and non differential output signals, and this was the one chosen.

3.4.3 Setup

To connect the CompactRIO to the driver boards the signal levels has to be adapted, the CompactRIOs digital input/output voltage is $+5V$ and the Skyper 32 driver has $+15V$ input/output signals. The adaptation is done by using a MC14504B "Hex Level Shifter for TTL to CMOS or CMOS to CMOS", the device is capable of shifting the voltage up or down depending on the supply voltages V_{CC} and V_{DD}. The circuit seen in figure 3.2a takes one CompactRIO output signal for each IGBT and level shifts it, the high voltage side is linked to the ribbon cable connectors that are connected to the driver boards.

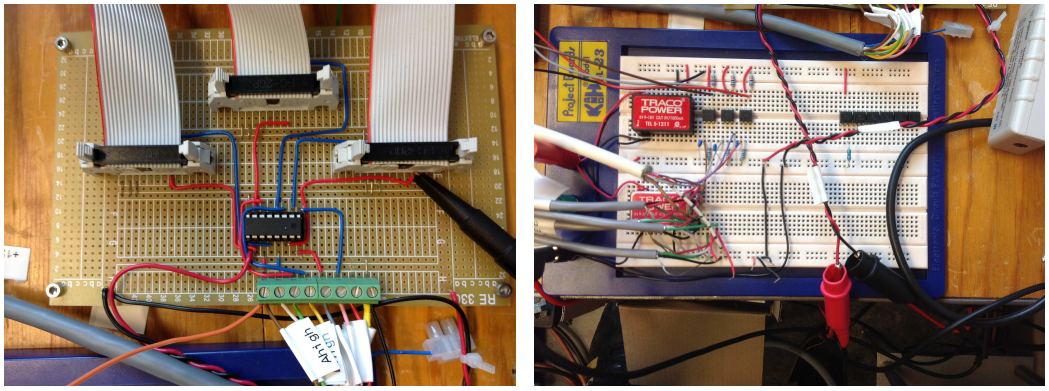

(a) Logic level shifter and connections to driver boards.

(b) Power distribution and isolation board.

Figure 3.2: Power distribution and logic level shifting boards.

Figure 3.2b shows a prototype board with two DC/DC converter and three optocouplers, the bottom DC/DC converter supplies the current sensor with $\pm 15V$ and the encoder with $+30V$. The top DC/DC converter supplies the optocouplers output side with $+5V$, the optocouplers level shifts the encoder $+30V$ output signals to $+5V$ for the CompactRIO.

Figure 3.3a shows the IGBTs and two of the driver board mounted on the heat sink, a $50\mu m - 100\mu m$ thin layer of thermal compound is applied between the IGBTs and the heat sink to improve thermal transfer. Figure 3.3b shows the snubber capacitors mounted on the IGBTs and the connection wires between the driver boards and the IGBTs, the wires should be twisted for noise rejection and the length should be kept as short as possible[23].

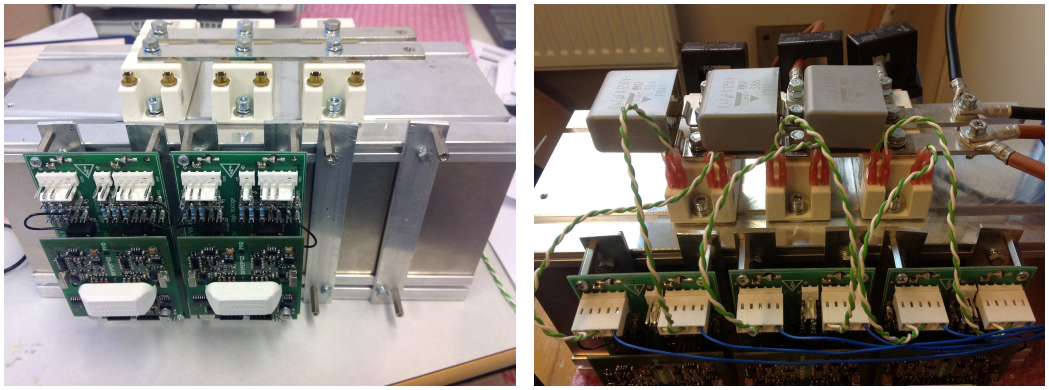

(a) Driver boards and IGBTs mounted on the heat sink.

(b) Driver boards connected to the IGBTs.

Figure 3.3: Drivers, IGBTs and snubbers.

Figure 3.4a shows a side view of the heat sink and component assembly. The currents sensors are shown in figure 3.4b with the motor phase wires passing through them, the sensor outputs are connected directly to the CompactRIOs analog input module.

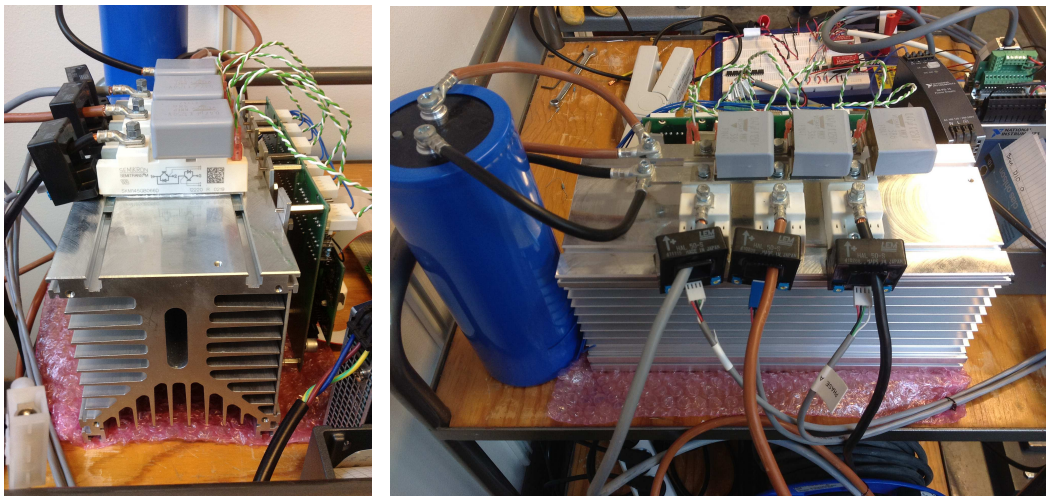

(a) Side view of heat sink.

(b) Current sensor on the motors phase cables.

Figure 3.4: Heat sink and current sensors.

Figure 3.5 shows an overview of the motor setup, figure 3.5d shows the encoder mounted on the motors shaft. The encoders rotating part is locked to the shaft with two grub screws and the fixed part is held on to the bearing support with a magnet for easy adjustment. To match the zero point of the motor with the encoder a wire was wound around the motor shaft, the wire was then connected to a scale to measure the torque. The inverter was then set to maximum output and a feed with a low DC voltage around 8-10V, where the encoder was turned to produce maximum torque for a minimum DC current.

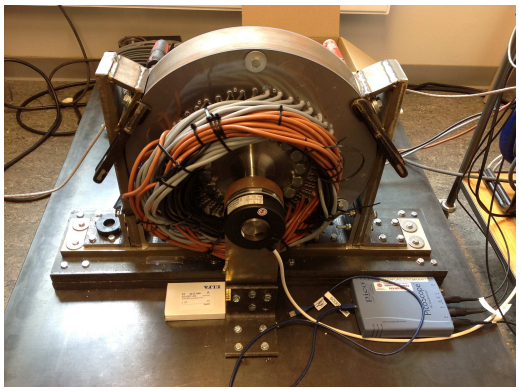

(a) Front view.

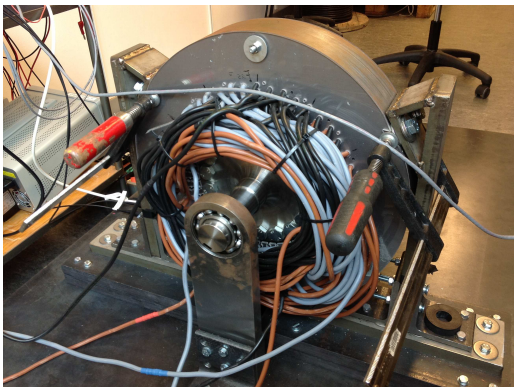

(b) Back view.

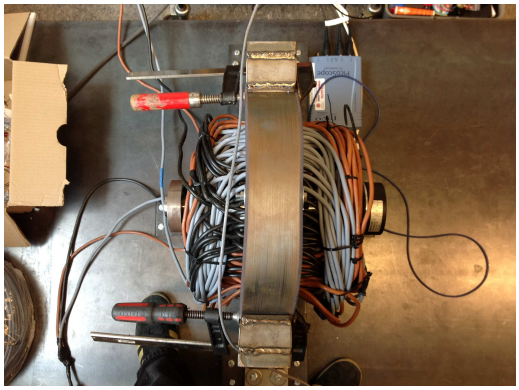

(c) Top view.

(d) Encoder

Figure 3.5: Overview of the Boel motor.

The motor is Y-connected to the inverter with the center point floating, an overview of the whole experimental set up is shown in figure 3.6.

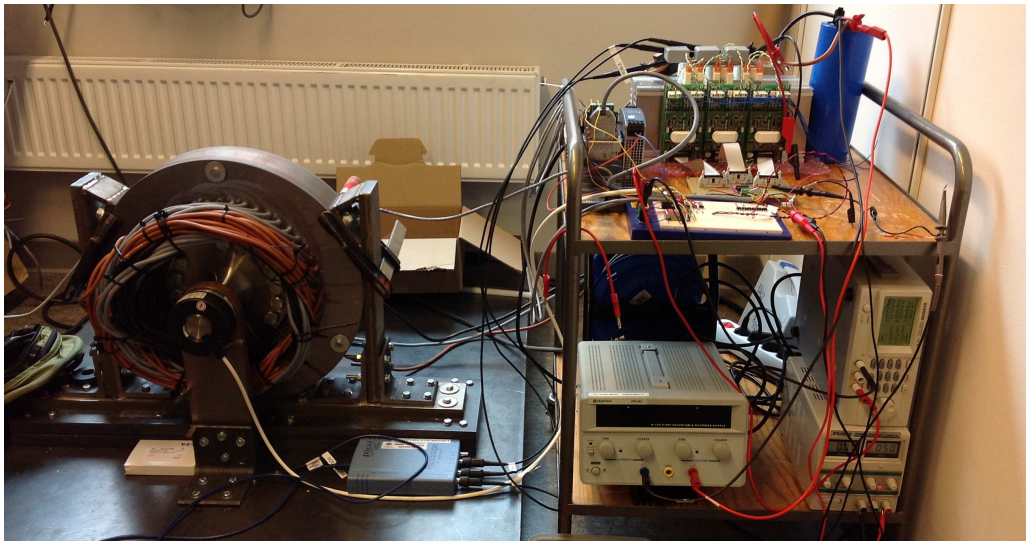

Figure 3.6: Overview over test set up.

Chapter 4

Software Implementation

4.1 Introduction

The software implementation consists of two parts, the control algorithm and the user interface. Most of the VIs used is available in the SoftMotion and FPGA Math & Analysis modules.

4.2 LabVIEW Code

Figure 4.1 presents the angle calculation loop. It is short enough to run during one single cycle timed loop, but in reality it will take two iteration to execute since the encoder block contains some feedback nodes. To get an accurate angle it is important to keep the loop frequency higher than the pulse frequency from the encoder. Two iterations are equal to 50ns or 20MHz on the 40MHz FPGA while the pulse frequency is 102.4kHz at 3000rpm with a 2048ppr encoder.

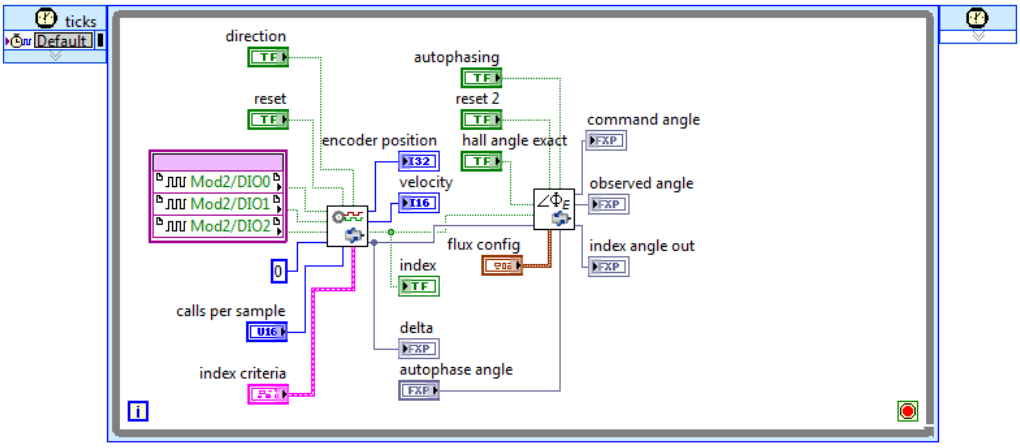

Figure 4.1: Encoder inputs to angle calculation.

Figure 4.2 presents the current measurement, filtering and the FIFO loop, the function reads the analog inputs from the current sensors and multiplies them with a factor that depends on the needed scaling and base current to get a normalized current. A lowpass filter is applied to filter the signal before the phase current is feed out from the loop as IphA reg, IphB reg and IphC reg. The two bottom case statements are used for turning the filter off and setting the measured current to zero. By setting the measured current

and the integrating part of the regulator to zero it is possible to bypass the function of the current PI regulators, they will only multiply the input the proportional part of the regulator.

The other part of the loop is the FIFO buffers. The FIFO is used to transfer blocks of data from the FPGA to the host computer. This loop consist of two FIFO buffers utilized to transfer the phase-, $\alpha\beta-$ and dq-currents to the host system.

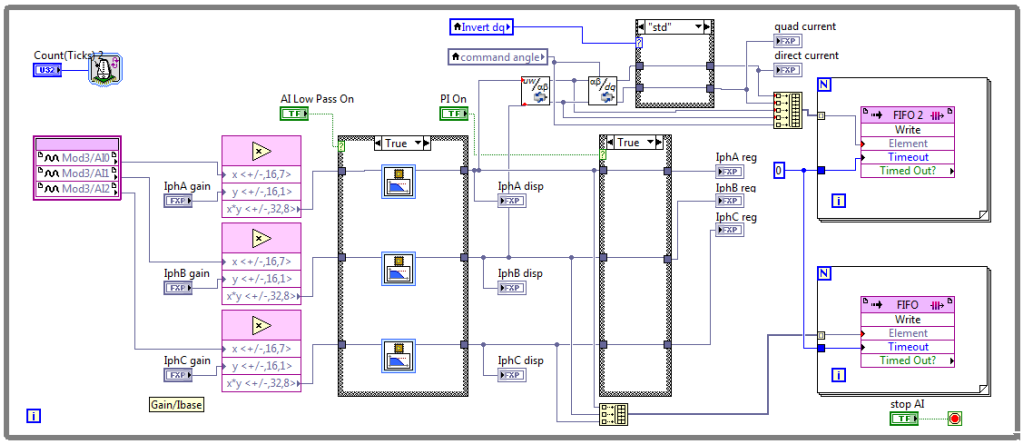

Figure 4.2: Current input, filtering and FIFO buffer.

Figure 4.3 presents then MTPA loop, because of the complexity of the current calculations two lookup tables are used instead of recalculation of a new value for every iteration. The d and q current values are generated in a separate initialization VI (figure 4.9) according to the equations 2.33 and 2.34. The input to the loop is a torque request and the output is the corresponding normalized direct and quadrature currents.

The motors rated torque is around 20nm and the control systems maximum torque has set to 64nm to allow for some over load situations. The lookup table consists of 1024 elements, so the maximum torque is multiplied with 16 to fill the whole table.

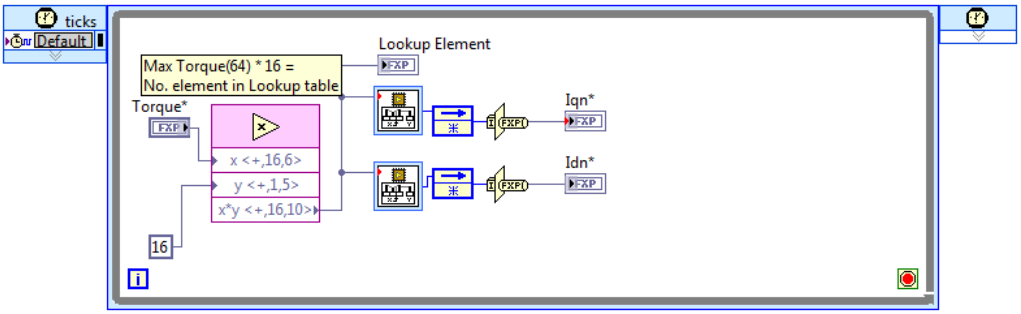

Figure 4.3: Look up table for MTPA current trajectories.

Figure 4.4 presents current request to duty cycle loop, by changing the case statements three different input types are available.

- Table - Uses the direct and quadrature currents from the lookup tables described above, the control reference is torque.
- Manual - Uses the $i_d = 0$ strategy for non-salient motors, the control reference is the quadrature current.
- Speed - Uses the speed PI loop as control reference.

The two measured phase current feedback values are transformed into direct and quadrature currents and is then feed into two individual PI regulators for current control, the feedback is compared with the current request and a direct and quadrature voltage set point between -1 and 1 is calculated by the PI VI. These voltages are then together with the rotor angle feed into an inverse Park transform that generates the α and β voltage inputs for the Space Vector Modulation VI, the SVM VI then outputs the duty cycle for the high side switches for each phase.

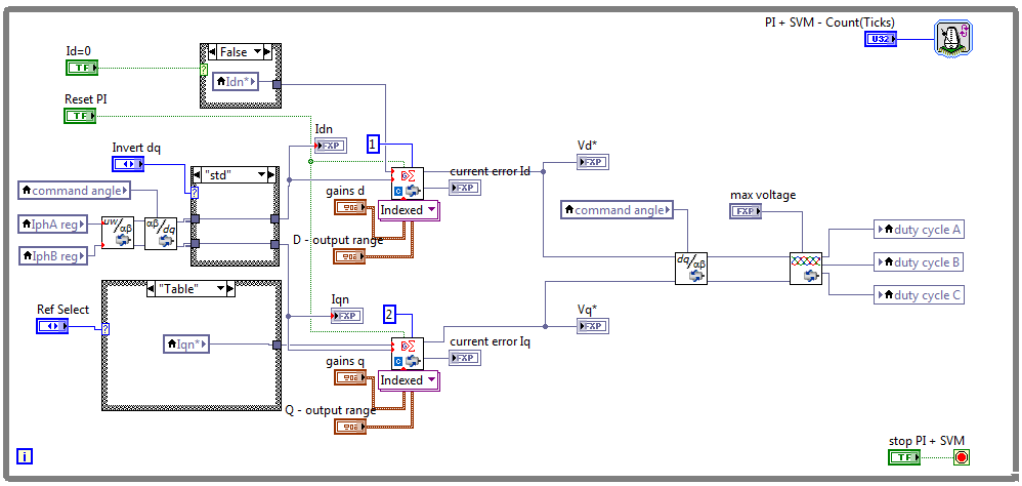

Figure 4.4: Current request to Duty cycle.

The SVM VI from National Instruments is somewhat different than the method described in the theory section, the difference lays in the sector determination and X, Y, Z values defined in equation 2.42. Figure 4.5 shows the first part of the SVM VI, it takes the requested α and β voltages as input and uses them to determine the sector. The case structure together with the addition in the next loop represents the duty cycle values t_1 and t_2 in the different sectors according to table 2.4, the difference from the theory part is that the X, Y, Z from the VI is twice as big.

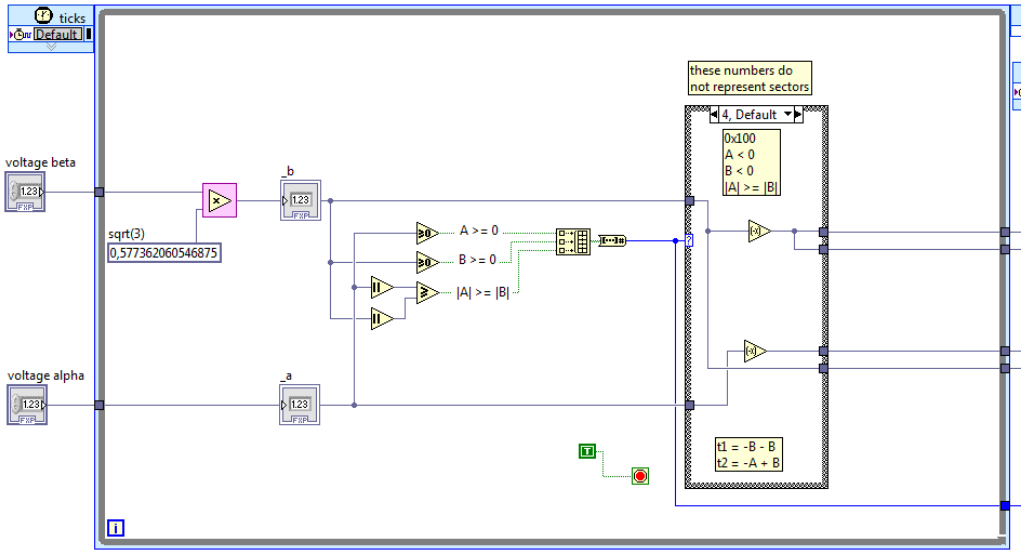

Figure 4.5: Space vector modulation VI, part 1.

The last case structure is used to assign the correct duty cycles to the correct inverter legs.

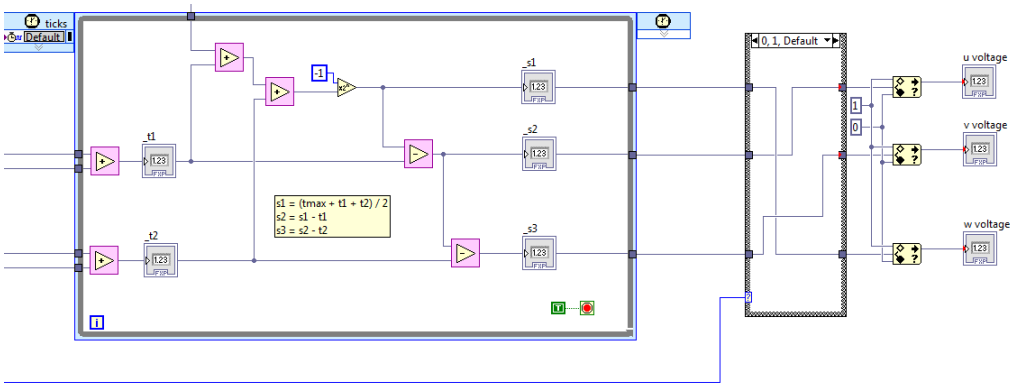

Figure 4.6: Space vector modulation VI, part 2.

Figure 4.7 presents the PWM loop, it contains one PWM timer VI for each phase and a case statement for setting all switches to off. The inputs signals are the duty cycles from SVM block, the desired switching frequency and PWM alignment selection. The PWM VI outputs are then split into two, where one of them is inverted to drive the low side switch for each phase. The full set of PWM signals are the feed out to the CompactRIOs physical outputs.

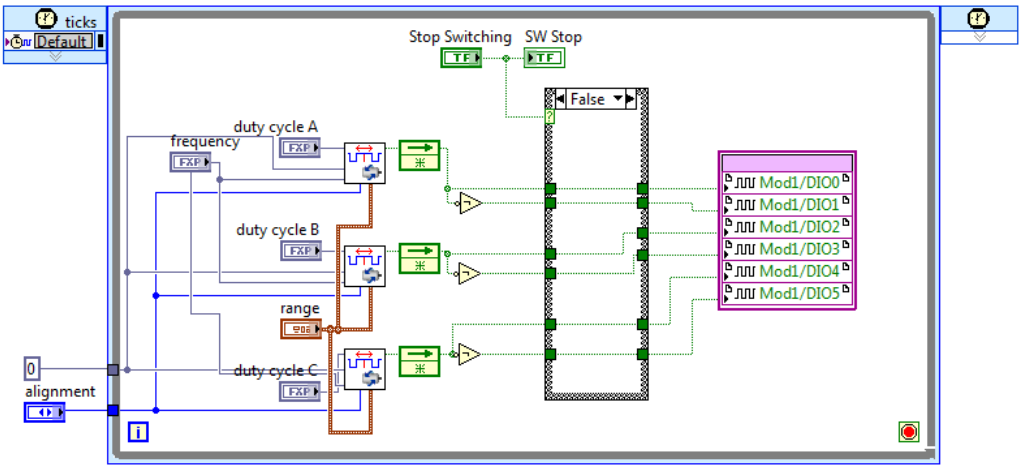

Figure 4.7: PWM output.

Figure 4.8 presents the speed control PI loop, using the ratio between the number of counted pulses and the loop rate as reference signal and outputs a current set point to achieve the requested speed.

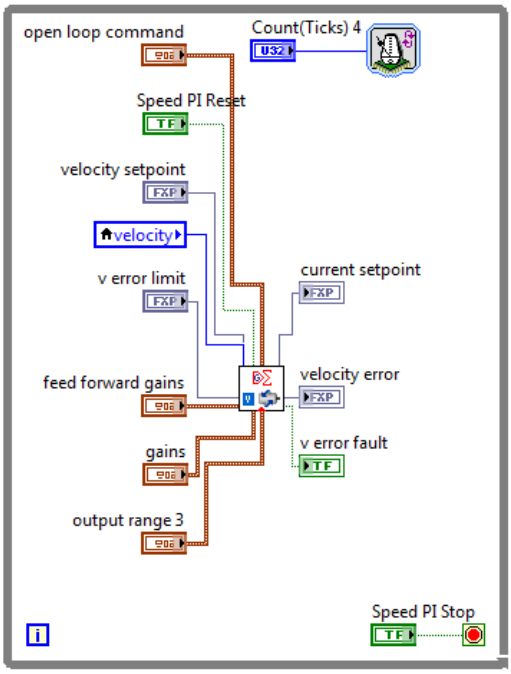

Figure 4.8: Speed PI control.

4.2.1 Generation of Lookup Tables

The generation VI of the lookup table for MTPA is not a part of the program running on the CompactRIO, it is only executed once during the programming phase and the result is stored in the memory when the rest of the program is uploaded to the CompactRIO.

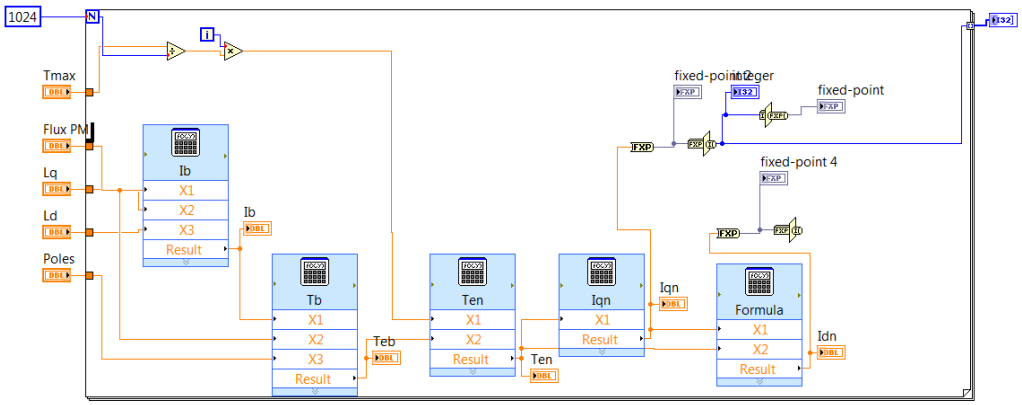

Figure 4.9: Lookup table generation VI.

Figure 4.9 presents the VI containing an input section for motor parameters and a math section for calculating the correct current trajectory, by rewiring the output terminal the same VI can be used for both tables. The math section implements equation 2.33 and 2.34 by using the Formula Express VI. Since this VI is using floating point numbers and the Lookup table only can store integers a conversion of the output is needed. This is done by using the "To Fixed-Point" and "Fixed-Point to Integer Cast". The integer is then converted back to fixed point in the main program by using the "Integer to Fixed-Point Cast", see figure 4.3.

4.3 User Interface

The user interface is created automatically when placing controls in the G code, figure 4.10 shows the selection of input method and the setpoint for either torque or quadrature current.

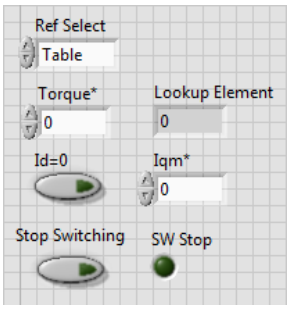

Figure 4.10: Torque or current request settings.

Figure 4.11 shows the current PI and measurement settings, the PI gains is set in gain input and the maximum output values from the regulator is set in the output range settings. The inputs from the current measurements are scaled to normalized current with the IphX settings. Figure 4.12 shows the speed PI control settings, the PI gains are set in

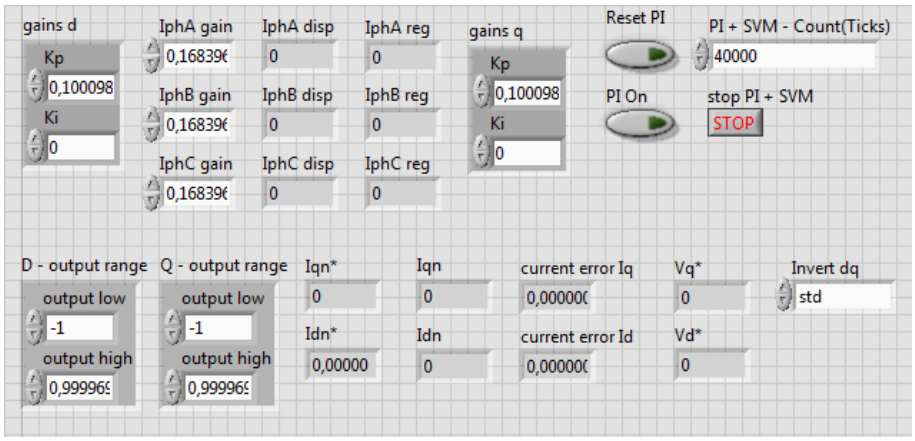

Figure 4.11: Current PI settings.

the gains settings and the speed in the velocity setpoint. The speed unit is in counts per execution cycle.

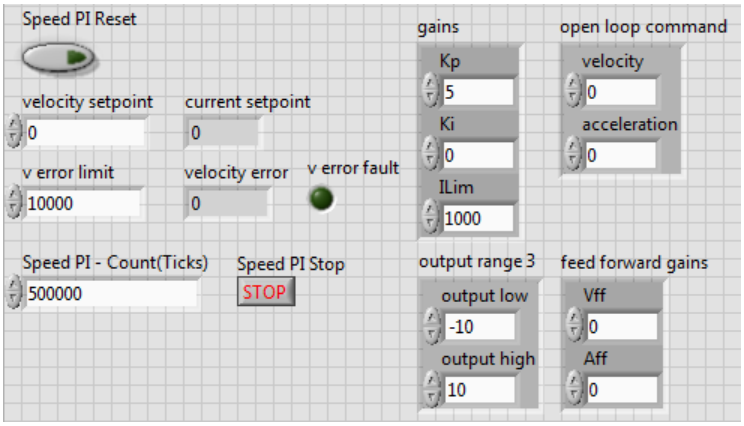

Figure 4.12: Speed PI settings.

Figure 4.13 shows the encoder settings. The index criteria sets the condition for the index pulse, in this case the index occurs when all three signal is high. The index angle is used to set the angle between the index position and the zero point of the motor. The angle increment is used to set the angle per encoder count according to

$$inc = \frac{rev}{ppr * X} = \frac{2}{2048 * 4} \approx 0.000244141 \tag{4.1}$$

where rev is the value for one revolution, ppr is the number of pulses per revolution and X is the encoding type. Figure 4.14 shows the PWM settings, the frequency setting set

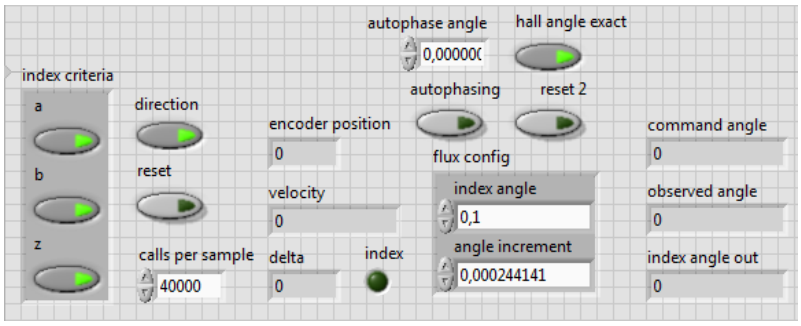

Figure 4.13: Encoder settings.

the switching frequency

$$f = \frac{f^*}{f_{fpga}} \tag{4.2}$$

where f^* is the desired switching frequency and f_{fpga} is the fpga execution frequency. The alignment setting changes between left- of center- aligned pulses. The minimum and maximum duty cycle is set with the range settings.

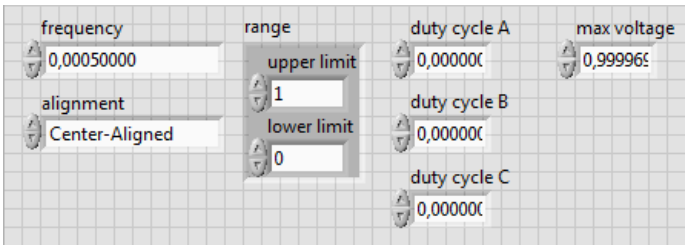

Figure 4.14: PWM settings.

Chapter 5

Results

5.1 Introduction

All measurements has been done with the current control turned off, the direct-axis voltage set to 0 and a maximum PWM duty cycle of 1. The DC-link voltage has been set to 60Vdc, which gives a maximum speed around 1200 rpm at maximum quadrature-axis voltage. Measurements of voltage, currents and their spectrums where done at five different speeds, no significant differences where shown and therefore only three of them are shown below.

5.2 Hardware

5.2.1 Signal Filtering

The output from the inverter will be a set of square wave pulse width modulated signals with variable duty-cycle. These square waves will average to the desired output voltage, the frequency of the PWM signal is between 5-20 kHz making the interpretation of the signal hard. All phase voltage and phase current measurements are therefore filtered with the oscilloscopes built in filter with a 1 kHz low-pass filter unless nothing else is mentioned. Figure 5.1 shows the same measurement both unfiltered and filtered. All spectrums has been calculated from unfiltered data.

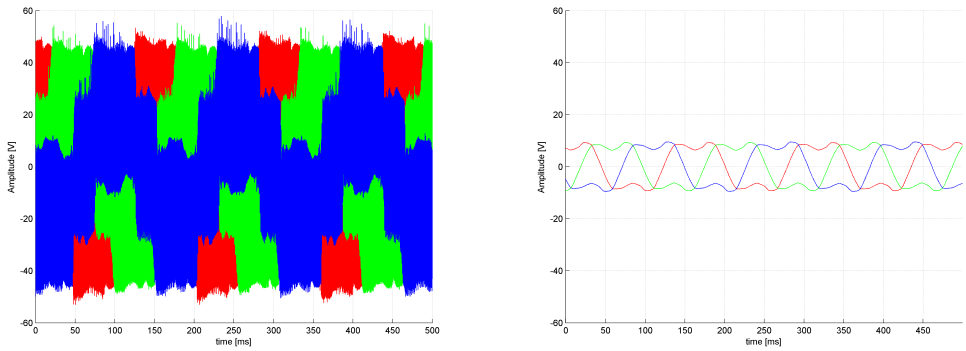

(a) Unfiltered

(b) 1kHz Low Pass Filter

Figure 5.1: Phase voltage at 367rpm.

5.2.2 367rpm

At 367rpm the phase voltage measurements (figure 5.2a) shows an asymmetric voltage where the first peak is lower than the second, this asymmetry is also seen in the calculated line voltage as a deformation at the peaks. The line voltage needed to reach 367rpm is $17V_{peak}$.

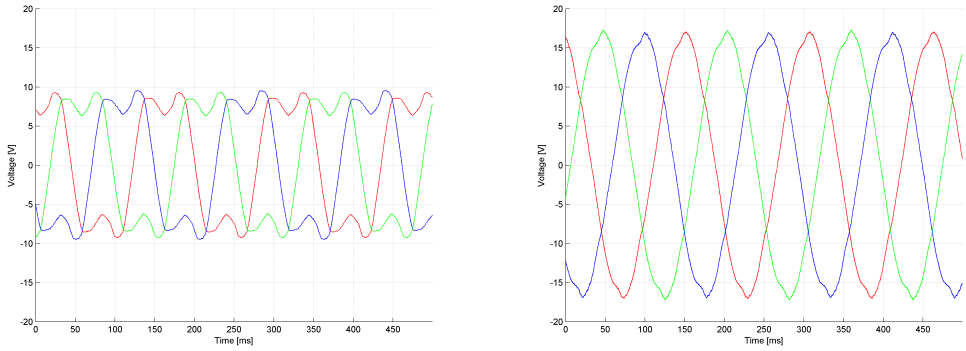

(a) Phase voltage (b) Line voltage

Figure 5.2: Phase and line voltage at 367rpm.

Figure 5.3 shows the phase and line voltage spectrums from 0 to 200Hz. The amplitudes for the fundamental frequency and the most significant harmonics is shown in table 5.1.

Table 5.1: Phase and line voltage harmonics.

Frequency	**Phase**	**Line**
Fundamental	17.4dBm	22.1dBm
3rd	-8.1dBm	-24.2dBm
5th	-16.4dBm	-12.0dBm
7th	-21.6dBm	-16.8dBm

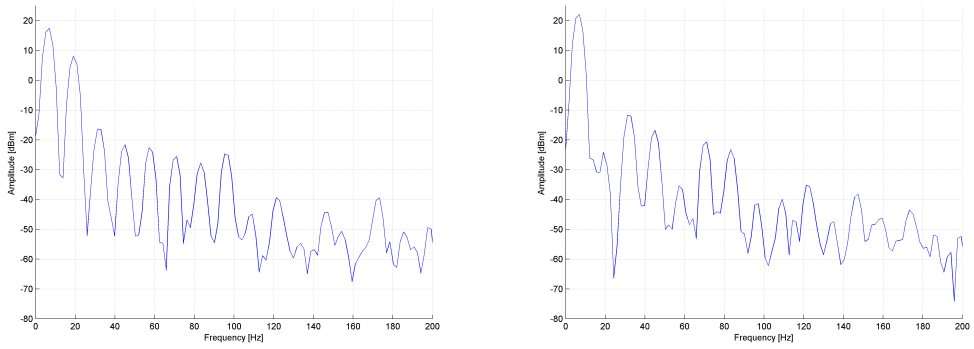

(a) Phase voltage spectrum (b) Line voltage spectrum

Figure 5.3: Voltage spectrum up to 200Hz at 367rpm.

Figure 5.4 shows a measurement over the phase current and its spectrum. The phase current shows deformations around zero- and peak- current, the peak current needed to

reach 367rpm is $400mA_{peak}$. The spectrum shows the fundamental peak as -16.0dBm, a 3rd harmonic of -36.3dBm, a 5th of -24.7dBm and a 7th of -35.9dBm.

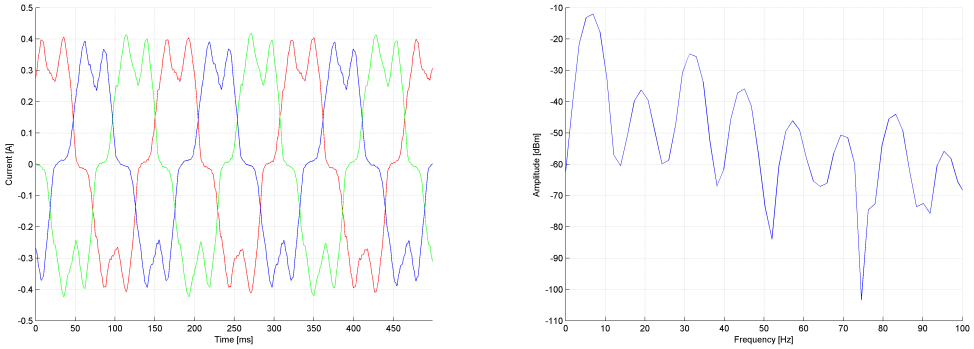

(a) Phase current (b) Phase current spectrum up to 200Hz

Figure 5.4: Phase current and spectrum.

5.2.3 665rpm

At 367rpm the phase voltage measurements (figure 5.5a) shows a near symmetrical phase voltage where both peaks have the same amplitude, as expected from the theory. Figure 5.5b shows the calculated line voltage of the same measurement. The line voltage needed to reach 665rpm is $28.4V_{peak}$.

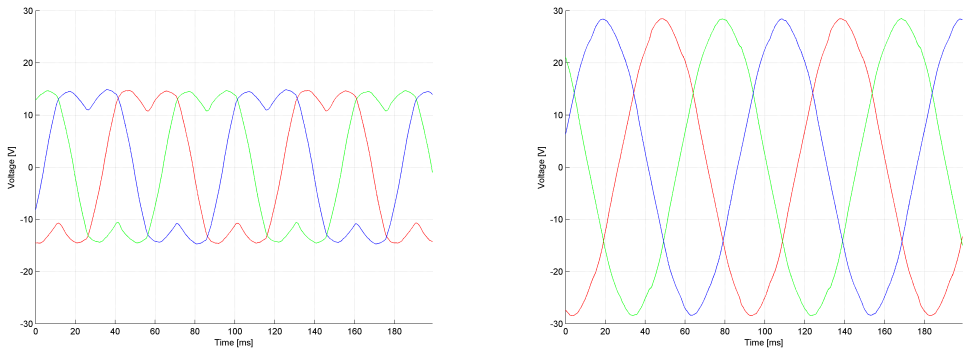

(a) Phase voltage (b) Line voltage

Figure 5.5: Phase and line voltage at 665rpm.

Figure 5.6 shows the phase and line voltage spectrums from 0 to 200Hz. The amplitudes for the fundamental frequency and the most significant harmonics is shown in table 5.2.

Table 5.2: Phase and line voltage harmonics.

Frequency	**Phase**	**Line**
Fundamental	21.0dBm	25.7dBm
3rd	10.1dBm	-32.0dBm
5th	-24.9dBm	-18.8dBm
7th	-16.5dBm	-12.2dBm

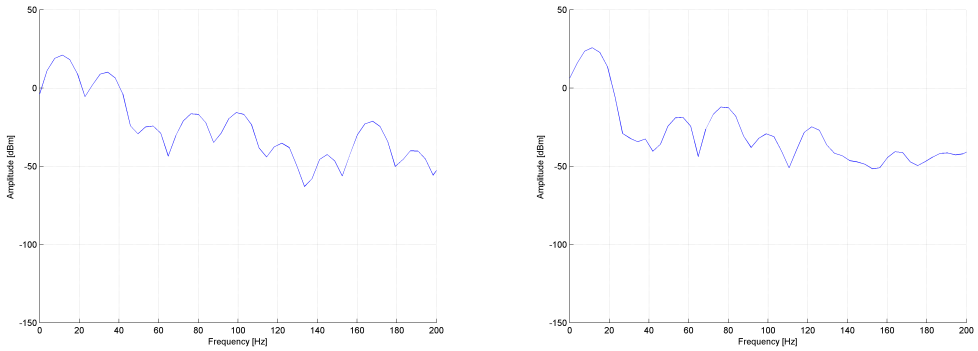

(a) Phase voltage spectrum (b) Line voltage spectrum

Figure 5.6: Voltage spectrum up to 200Hz at 665rpm.

Figure 5.7 shows a measurement over the phase current and its spectrum. The phase current shows deformations around zero- and peak- current, the peak current needed to reach 367rpm is $0.75A_{peak}$. The spectrum shows the fundamental peak as -7.2dBm, a 3rd harmonic of -34.5dBm and a 5th of -20.9dBm.

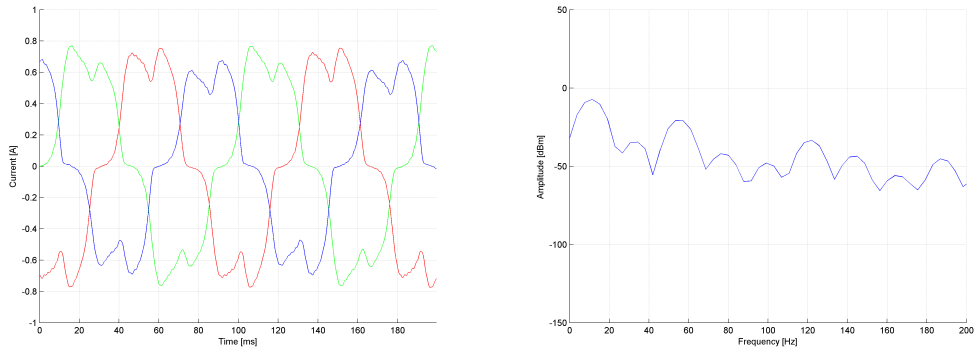

(a) Phase current (b) Phase current spectrum up to 200Hz

Figure 5.7: Phase current and spectrum.

5.2.4 1217rpm

At 1217rpm the phase voltage measurements (figure 5.8a) shows an asymmetric voltage where the first peak is higher than the second, this asymmetry is also seen in the calculated line voltage as a deformation at the peaks. The line voltage needed to reach 1217rpm is $60V_{peak}$.

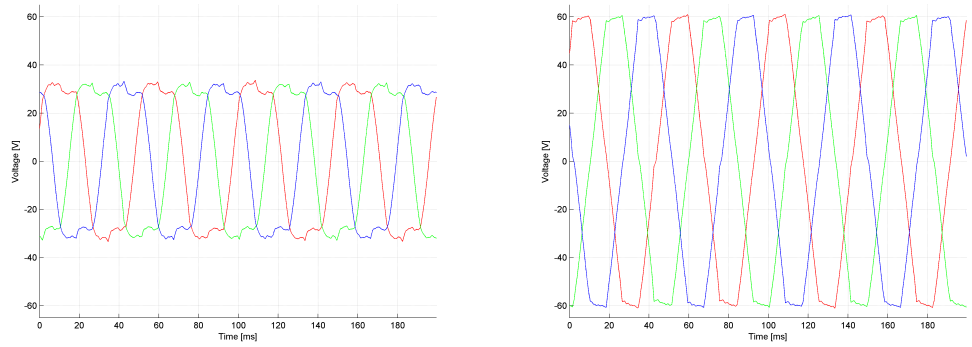

(a) Phase voltage (b) Line voltage

Figure 5.8: Phase and line voltage at 1217rpm.

Figure 5.9 shows the phase and line voltage spectrums from 0 to 200Hz. The amplitudes for the fundamental frequency and the most significant harmonics is shown in table 5.3.

Table 5.3: Phase and line voltage harmonics.

Frequency	Phase	Line
Fundamental	27.8dBm	32.6dBm
3rd	14.9dBm	-16.5dBm
5th	-0.9dBm	-5.4dBm
7th	-9.9dBm	-5.1dBm

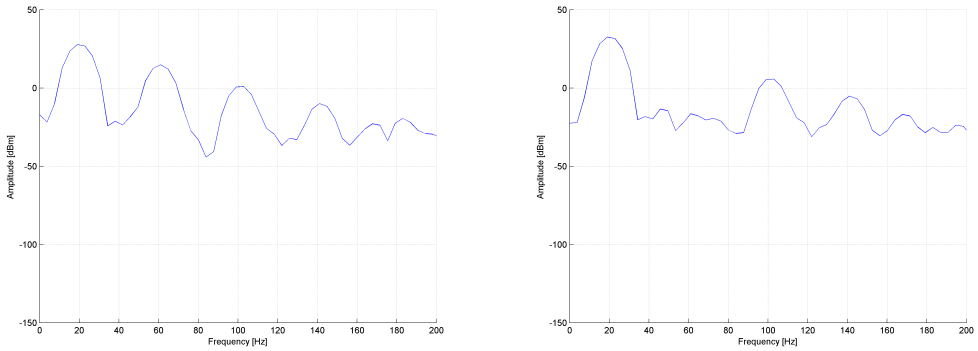

(a) Phase voltage spectrum (b) Line voltage spectrum

Figure 5.9: Voltage spectrum up to 200Hz at 1217rpm.

Figure 5.10 shows a measurement over the phase current and its spectrum. The phase current shows less deformations around zero- and peak- current than the previous mea-

surements, the peak current needed to reach 1217rpm is $6A_{peak}$. The spectrum shows the fundamental peak as 11.7dBm, a 3rd harmonic of -29.4dBm, a 5th of -15.0dBm and a 7th of -25.8dBm.

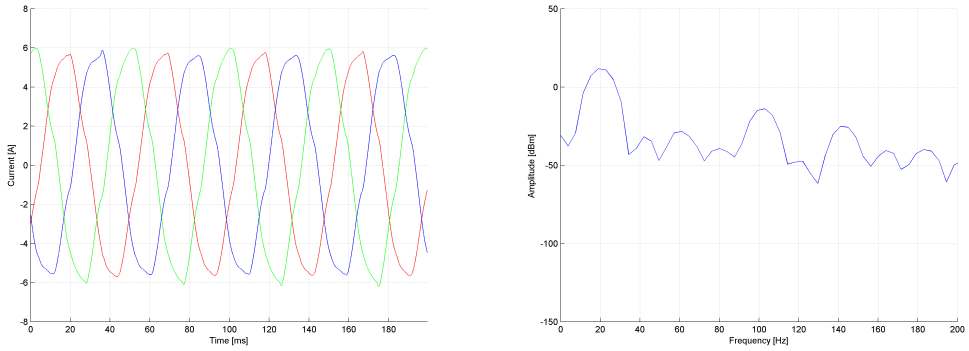

(a) Phase current

(b) Phase current spectrum up to 200Hz

Figure 5.10: Phase current and spectrum.

5.2.5 Switching

Figure 5.11 shows the effect of switching frequency on the ringing of the collector emitter voltage. At the lower frequency the ringing has time to settle down at the DC-link level, but at the higher frequency the ringing never settles between switching. All measurements of the switching behaviour has been done without signal filtering.

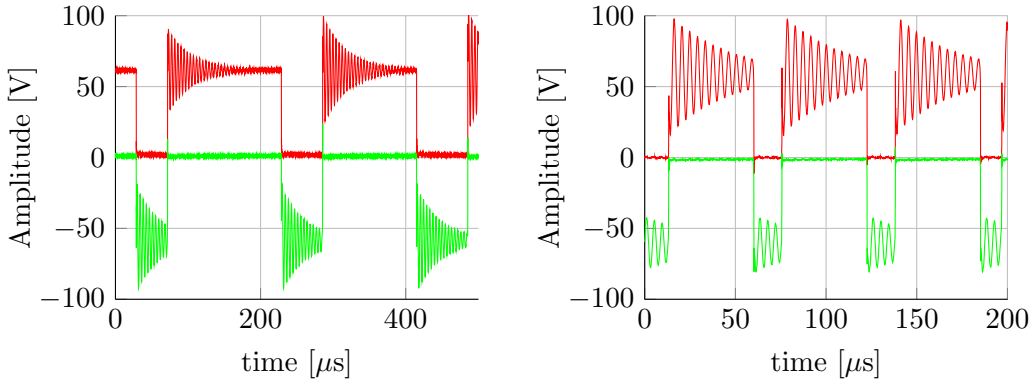

(a) 5kHz. (b) 20kHz.

Figure 5.11: Collector - emitter voltage vs switching frequency at 1217rpm.

Figure 5.12 shows the ringing as a function of speed, i.e. current. At low currents the ringing is small, but on higher current the ringing gets higher.

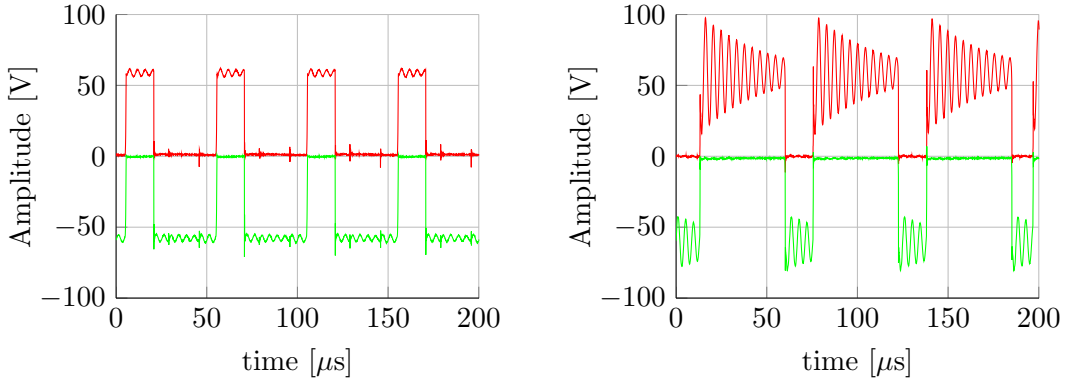

(a) 367rpm, 20kHz Switching Frequency. (b) 1217rpm, 20kHz Switching Frequency.

Figure 5.12: Collector - emitter voltage vs speed.

Figure 5.13 shows the ringing on the DC-link voltage at different currents and switching frequencies. Low current and high switching frequency is shown in 5.13a, the spikes in the graphs originates from the stray inductances when a switch is opened. In 5.13b the ringing is higher, the turn off times of the switches can be identified from the abrupt changes in amplitude.

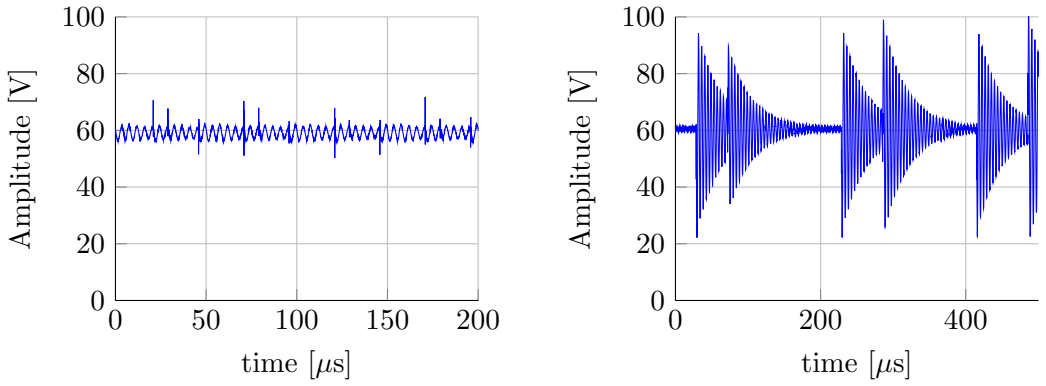

(a) 367rpm, 20kHz switching frequency.

(b) 1217rpm, 5kHz switching frequency.

Figure 5.13: DC-link voltage.

Figure 5.14 show the collector emitter voltage during turn on and turn off of both the high and low side switches of one phase, it also shows the DC-link voltage during the same time. Both the turn on and turn off time is approximately 100ns.

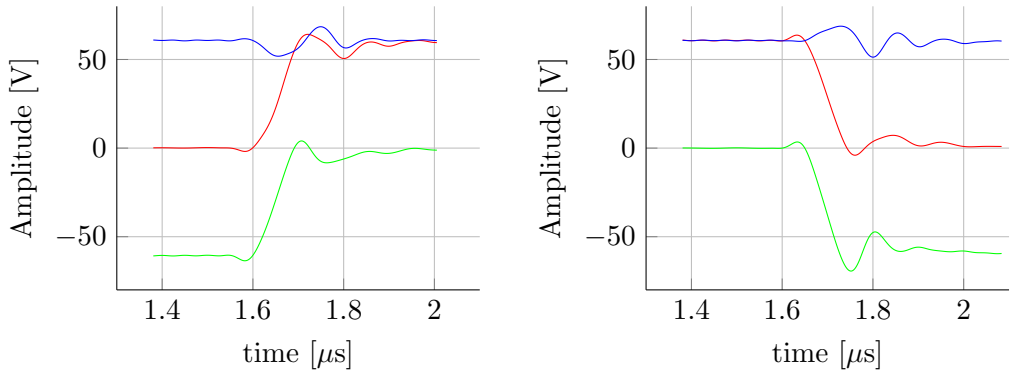

(a) Turn On/Off.

(b) Turn Off/On.

Figure 5.14: Turn On/Off Time at 131rpm and 20kHz.

5.2.6 Speed Vs Voltage/Current

Figure 5.15 shows the peak voltages and currents as a function of rotational speed over all five measurements. 5.15a shows that the speed increases linearly with the line voltage. 5.15 shows the current increasing quadratically as a function of speed.

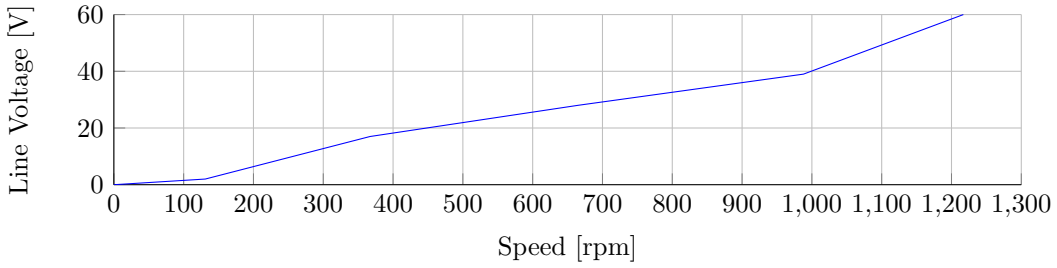

(a) Line voltage.

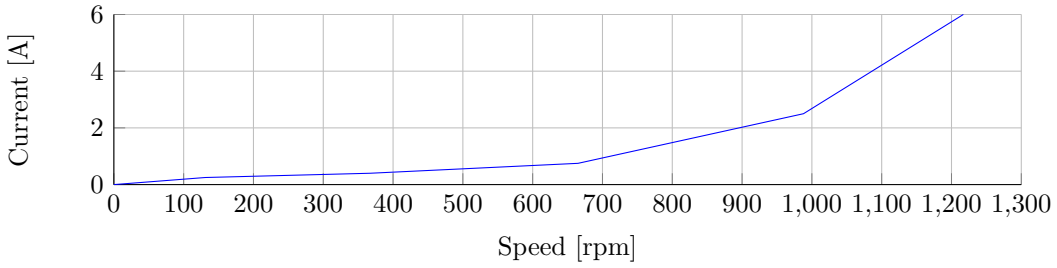

(b) Phase current.

Figure 5.15: Speed vs voltage and current.

5.2.7 Inductance Vs Rotor Angle

The indicated rotor angle in LabVIEW and the inductance of the phase winding c-n was measured and compared to determine if the encoder position was synchronized with the rotor position, figure 5.16 shows a plot over two measurements over the stator inductance as a function of rotor angle. The plot shows peaks at 0.9π radians and 1.9π radians, indicating that the encoder position is 0.1π radians out of phase from the peak inductance.

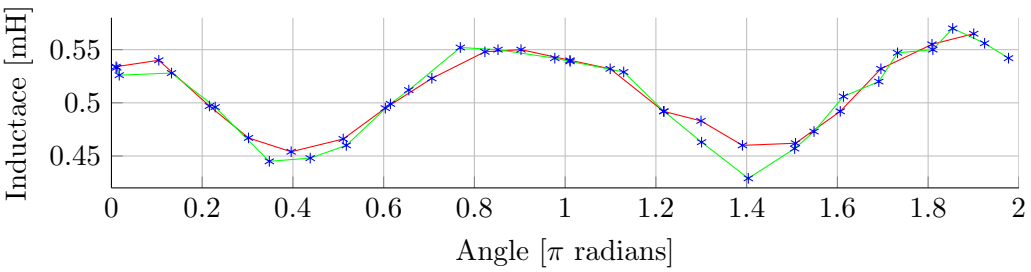

Figure 5.16: Stator inductance vs encoder angle.

Chapter 6

Discussion

6.1 Introduction

There are a lot of different parameters that can be changed in the system, all affecting the test result. Some of the constraints in the lab have also limited what could be tested. One of them is the lack of a load for the motor, the only torque produced is just as high as to overcome the motors mechanical losses. The $I_d = 0$ control strategy was therefore used, since the MTPA curve current lies close to parallel to the q-axis at low torque. Another constraint is the motors mechanical construction, it seem to have a natural frequency at around 1500 rpm and does have some vibrations there. The only time it was taken up to 2000 rpm it made a clonking noise, this has limited the measurement range to below 1200 rpm. Another limitation has been the control system, the PI current controllers has not worked. Therefore all measurements have been done by controlling the direct- and quadrature-axis voltage.

None of the tests and measurements of the small-scale inverter has documented, but the experiments showed that the development of the control was on the right track.

6.2 Software

The software design has been fairly straight forward. Use of LabVIEW has simplified both the programming process and the creation of a user interface for the inverter. The threshold for getting started with programming the CompactRIO with LabVIEW seems much lower than for programming a MCU with C. A drawback of the FPGA has been the long compile time, up towards 45 minutes. This could be an annoyance while testing new ideas, but it also make one think more thoroughly over every change made in the code.

6.3 Hardware

The selection of component has been simplified by using Semikrons design tool for the power components and using their gate drivers, other components such as the CompactRIO, current sensors and snubber capacitors has been chosen because they were already available in the lab. Another way of doing it would be to do all the calculation and simulate the circuit, but doing so would probably fill a whole master thesis by itself.

The intention was to use a driver board developed at the university, but they were in the process of finishing a new board layout when the drivers were needed. So a decision

was made to use a commercial driver to be sure of not ending up with a driver with a possible design fault.

The support electronics i.e. DC/DC converters, optocouplers, etc. would need to be moved from the temporary development boards to a custom made PCB for the task. Some work with signal filtering should also be done, for example the low pass filtering of the current signals could be done with passive components instead of digitally in the CompactRIO to save some gates.

6.4 Measurements

The measurements done shows that the SVM design is working, in the 665rpm case the phase voltage looks close to the ideal theoretical shape. The low speed measurement shows a phase voltage where the right peak is higher than the left, the high speed shows the opposite. The reason for this displacement could be interesting to investigate further to see if it is originating from the control or from the motor, this could be done by testing the same speeds/loads with different DC-link voltage with an output modulation to match the old measurement load. Looking at the low frequency spectrum of the phase voltages, it is clear that all measurements contain a significant third harmonic. This is what was expected from the theory, but the high speed measurement also contains a fairly large 5th and 7th harmonic. The reason for that can best be seen in the line voltage plot, the control system has reached maximum voltage limit and the line voltage peaks has been flattened to form a more trapezoidal shaped voltage.

The phase currents for the two slowest measurements show a significant counter rotating 5th harmonic, while in the high speed measurement the 5th harmonic is much smaller. The 5th harmonic causes a counter electromotive force (CEMF) that will counteract the motors torque, it is therefore important to minimize this harmonic.

The switching measurements shows significant ringing with both 5kHz and 20kHz switching frequencies at higher currents, the capacitor only snubber is clearly not enough to dampening the ringing. This would probably be a problem at higher voltage and currents, where the ringing possibly could exceed the rated voltage of the IGBT. The first step for reducing the ringing would be to reduce stray inductance in the power supply circuit, this could be done by shortening the cables between the power supply and inverter. Installing a larger capacitor bank directly on the DC bus bars and using laminated bus bars would also help. If this doesn't help, more advanced snubbers such as RC or RCD might be needed. Another way to reduce the ringing is to increase the gate resistance, especially the turn off resistance. Both snubbers and slower switching speeds will introduce more losses in the system, which solution that is the best will have to be tested or simulated to achieve the smallest losses.

The turn on and turn off time measurement is one that could be questioned, the measurement shown in figure 5.14 is done with a 20MHz Picoscope and shows a turn on/off time of approximately 100ns. The bandwidth of the scope is probably too low for capturing the voltage spikes at switching and it doesn't sync on the edges, so it is hard to tell if the time is constant or varies over time. 100ns turn off time is much faster than the typical time specified in the data sheet for the IGBT, increasing the gate resistance to lower the turn off time might reduce the ringing.

As seen in figure 5.15 the speed shows a linear increase with increasing voltage. The current however, looks to have an quadratic increase. Doing a quadratic interpolation in Matlab shows that the peak current will reach $47.9A$ at 3000rpm, this is equivalent to $33.9A_{rms}$. A plot of the interpolation can be seen in appendix B. The high no load

current at higher rpm's indicates high losses in the motor.

Figure 5.16 is indication that the encoder is positioned 0.1π radians before the center of the pole, but looking at figure 4.13 it can be seen that the encoder angle is advanced by 0.1π radians during the measurement. This adjustment was done because the motor seemed to produce a higher speed/torque at the same current with the encoder angle advanced a bit. However, no real measurement of this was done. It was more done by the eyes and ears of the author, so the result might not be completely truthful. However, the method of measuring the stall torque and current while turning the encoder seems to produce a correct estimation of the zero point of the motor.

Chapter 7

Conclusion

7.1 Introduction

Overall this has been a successful project even though there have been some setbacks and limitations in available equipment. A working power electronics unit has been constructed for an inverter. The electronics has been proven to work for low currents and low voltage, but an improved lab set up with the possibility to test the inverter using rated voltage and current is needed to fully confirm its function. The space vector modulation control algorithm has been proven to work for PSPMSM.

What has not worked is the current control with the possibility to use torque as the input reference value. The ringing will likely increase as the current go

7.2 Future Work and Improvements

7.2.1 Motor Construction

As seen in figure 3.5 this is an experimental motor that still needs some work. The only easy solution for placing the encoder was on the output shaft, thus preventing a connection between the motor and a future load. There is room to move the encoder on the inside of the rear support bearing, there is also a possibility to move the rear bearing support closer to the stator to get a output shaft on both sides of the motor.

7.2.2 Load Test

To properly test the Inverter and motor and verify the FOC and MTPA theory it would be necessary do it under different load conditions. The load could for example be agenerator, a large flywheel or some kind of brake system. A larger DC source capable of the motors rated current and voltage values will also be needed.

7.2.3 Current Control

To be able to control the torque and implement MTPA control a functional current control needs to be implemented.

Appendix A

SKYPER 32PRO R Driver Configuration

The Skyper driver needs to be configured according to the specific application, the configuration is done by adding external components. Using the adaptor board will simplify the set up since it already contains some electronics such as, input triggering, temperature monitoring and fault management. However, some additional components are needed to adapt the driver behavior for the specific application.

The dead time is the time between switching of the high and low side switches where both switch signal are off. Dead time is needed to prevent shoot through, a condition where both switches are closed creating a short circuit between the DC terminals. The dead time is set with by adding or removing zero ohm resistors to the R43, R44, R45 and R46 pads on board. This makes it possible to set the dead time between 0 to 4.3μs in 9 steps. How to select the time can be seen on page 12 of the driver data sheet[24], where "GND" indicates a zero ohm resistor and "open" indicates no resistor. The R43 on the adaptor board is reference as "PRIM_CFG_TDT2_IN" in the driver data sheet, R44 as "PRIM_CFG_SELECT_IN", R45 as "PRIM_CDG_TDT3_IN" and R46 as "PRIM_CFG_TDT1_IN". The pads are located next to the control cable input and can be seen in figure A.1, the dead time is set to 3.3μs from the factory.

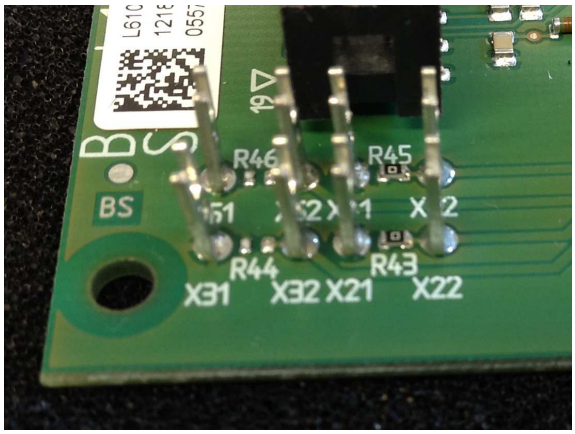

Figure A.1: Dead time resistors.

The adaptor board is equipped with an Over Temperature Protection Circuit (OTP), it can be used with IGBT modules with integrated temperature sensors or with external PTC or NTC resistors mounted to the heat sink. The turn off temperature is set by the

three resistors R172, R175 and R177 seen in figure A.2 and the values is calculated from the instructions on page 9 in the adaptor boards data sheet[25]. When no temperature sensor is used as in this application, R175 and R177 needs to be removed and R172 equipped with a zero ohm resistor.

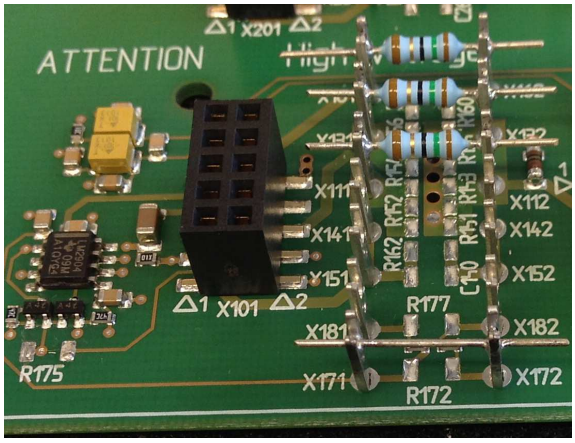

Figure A.2: Gate and temperature resistors.

The gate resistors will control the IGBTs turn on and turn off time, the adaptor board is designed to use three parallel MiniMELF SMD resistors for each gate resistor. There is also a possibility to use a standard resistor connected between the X connectors for quick changes during testing. The high side gate resistors (R151-156) is shown in figure A.2 and for the low side (R251-256) in figure A.3a. In total there is three resulting gate resistors for each switch, R_{Gon} for turn on, R_{Goff} for turn off and R_{Goff_SC} for soft turn off. The soft turn off is used when a short circuit is detected, the R_{Goff_SC} is then connected in series with R_{Goff} to make the turn off slower, thus reducing the voltage spikes generated by the stray inductances in the circuit.

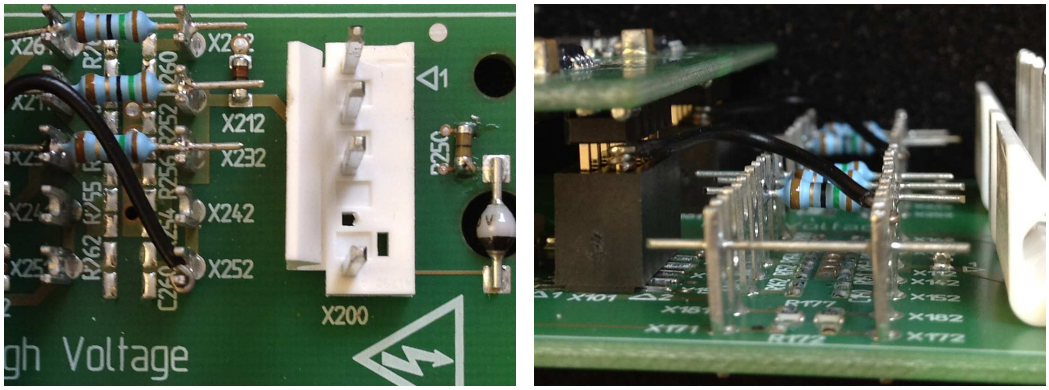

(a) Collector Emitter voltage measurements resistor and bypass wire.

(b) Collector Emitter voltage measurements bypass wire.

Figure A.3: Collector Emitter voltage measurement setup.

The Dynamic Short Circuit Protection (DSCP) function can detect a short circuit or over current in the circuit, this is done by comparing the Collector Emitter Voltage (V_{CE}) over the closed switches with the voltage over the RC circuits made up by R161, C150, R262 and C260. Calculations of the RC component values is shown on page 13 in the driver data sheet[24].

The V_{CE} is should be measured with a high voltage diode in series with a resistor, the diode is already on the board but the resistors R150 and R250 has to be mounted on the board. The resistors are selected as zero ohms for 1200V operation and 1k ohm for 1700V operation.

To disable the DSCP during the development phase, "SEC_TOP_VCE_IN" must be connected to "SEC_TOP_GND" and "SEC_BOT_VCE_IN" to "SEC_TOP_GND" according to page 13 in the driver data sheet[24]. Translated to the adaptor board the connections needed is a wire between the X142 or X152 to pin 2 in the X101 connector for the high side driver and a wire between the X242 or X252 to pin 2 in the X201 connector for the low side driver. The wires is shown in figure A.3.

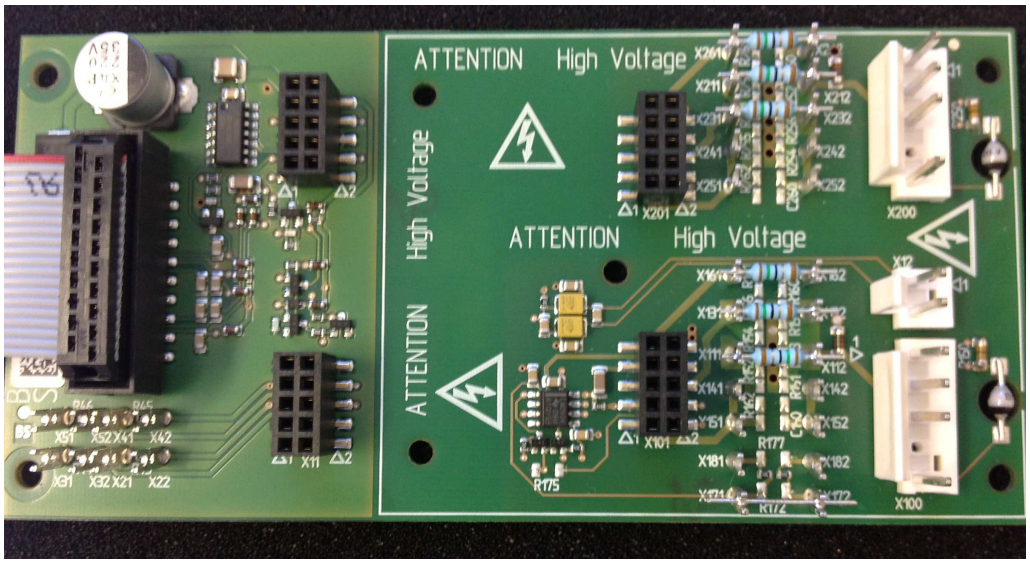

Figure A.4: Finished adaptor board.

Figure A.4 shows an overview of the assembled adaptor board and figure A.5 and A.3b shows the adaptor board with the driver mounted.

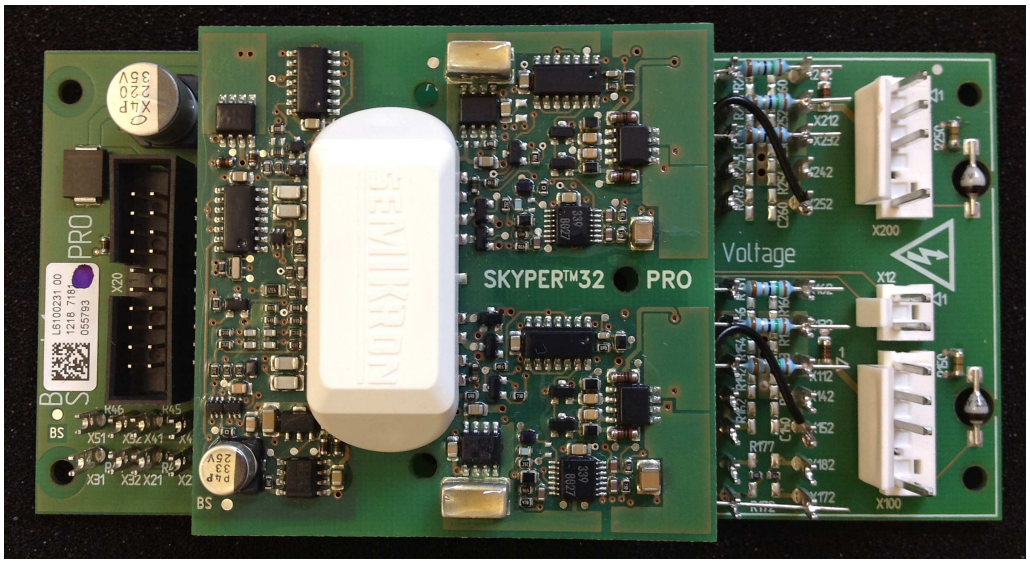

Figure A.5: Finished assembled driver.

Appendix B

Quadratic Interpolation of Phase Current vs. Speed

Quadratic interpolation of the phase current performed in matlab gives the following expression

$$y = p1 * x^2 + p2 * x + p3 * x \tag{B.1}$$

where

$$p1 = 6.4827 * 10^{-6}$$

$$p2 = -0.0036028$$

$$p3 = 0.37557$$

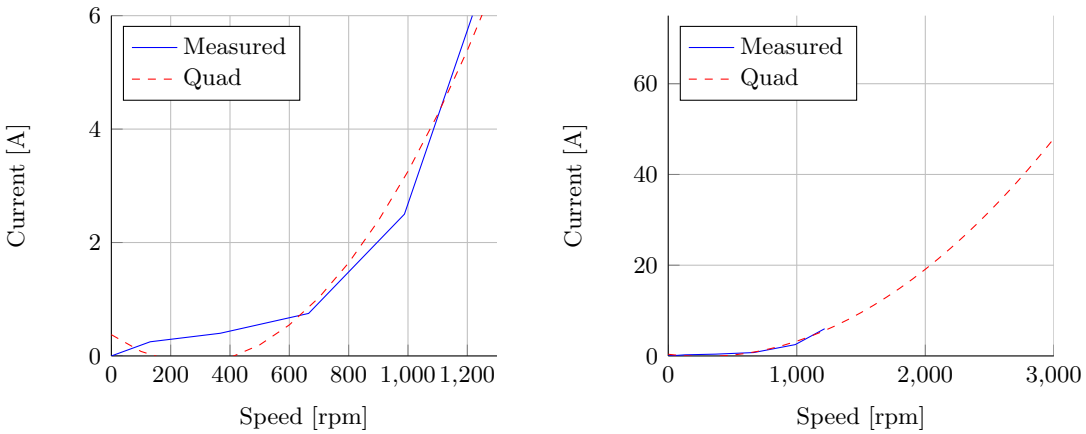

(a) Measured range.

(b) Extended range.

Figure B.1: Quadratic interpolation of phase current vs speed.

Bibliography

[1] J.G.W. West. Dc, induction, reluctance and pm motors for electric vehicles. *Power Engineering Journal*, 8(2):77–88, 1994.

[2] Janaína Gonçalves de Oliveira. *Power Control Systems in a Flywheel based All-Electric Driveline*. PhD thesis, Uppsala University, 2011.

[3] Anders Kronberg. Design and simulation of field oriented control and direct torque control for a permanent magnet synchronous motor with positive saliency. Master's thesis, Uppsala University, 2012.

[4] Pragasan Pillay and R. Krishnan. Modeling of permanent magnet motor drives. *IEEE Transactions on Industrial Electronics*, 35(4):537–541, 1988.

[5] Jacek F. Gieras. *Permanent magnet motor technology: design and applications*. Electrical and Computer Engineering Series. CRC Press, 2009.

[6] Boel Ekergård. 2012.

[7] Juha Pyrhönen. Electrical drives - lecture notes, 2011.

[8] M. Leijon, B. Ekergård, S. Ferhatovic, J. de Santiago, H. Bernhoff, R. Waters, and S. Eriksson. On a two pole motor for electric propulsion system. 2012.

[9] B. Bolund, M. Leijon, and U. Lundin. Poynting theorem applied to cable wound generators. *IEEE Transaction on Dielectrics and Electrical Insulation*, 15(2):600–605, 2008.

[10] Andreas P. Friedrich and Helmuth Lemme. The universal current sensor. `http://www.sensorsmag.com/sensors/electric-magnetic/the-universal-current-sensor-1029`, 2000.

[11] Jacob Fraden. *Handbook of Modern Sensors: Physics, Designs, and Applications*. Springer, 2004.

[12] National Instruments, `http://www.ni.com/white-paper/7109/en`. *Encoder Measurements: How-To Guide*.

[13] H. Abu-Rub, A. Iqbal, and J. Guzinski. *High Performance Control of AC Drives with Matlab / Simulink Models*. Wiley, 2012.

[14] Ned Mohan, Tore M. Undeland, and William P. Robbins. *Power Electronics Converters, Applications, and Design*. Wiley, 2003.

[15] Carl Blake and Chris Bull. *IGBT or MOSFET: Choose Wisely*. International Rectifier, `http://www.irf.com/technical-info/whitepaper/choosewisely.pdf`.

[16] Semikron, www.semikron.com/application/drivercalculation. *IGBT Driver Calculation*, 2007. AN-7004.

[17] Semikron, www.semikron.com/application/gateresistor. *Gate Resistor - Principles and Applications*, 2007. AN-7003.

[18] P.D. Chandana Perera, F. Blaabjerg, J.K. Pedersen, and P. Thogersen. A sensorless, stable v/f control method for permanent-magnet synchronous motor drives. *IEEE Transaction on industry applications*, 39(3):83–89, 2003.

[19] Edith Clarke. *Circuit analysis of A-C power systems.* John Wiley & sons, 1943.

[20] R. H. Park. Two-reaction theory of synchronous machines generalized method of analysis-part i. *Transactions of the American Institute of Electrical Engineers*, 48(3):716–727, July 1929.

[21] Thomas M. Jahns, Gerald B. Kliman, and Thomas W. Neumann. Interior permanent-magnet synchronous motors for adjustable-speed drives. *IEEE Transaction on industry applications*, IA-22(4):738–747, 1986.

[22] Texas Instruments. *Digital Motor Control*, 2003. SPRU485A.

[23] Semikron, www.semikron.com/application/driverconnection. *Connection of Gate Drivers to IGBT and Controller*, 2006. AN-7002.

[24] Semikron, http://www.semikron.com/products/data/cur/assets/Board_1_SKYPER_32PRO_R_L6100231.pdf. *Board 1 SKYPER 32PRO R*, 2010.

[25] Semikron, http://www.semikron.com/products/data/cur/assets/SKYPER_32_PRO_R_L6100202.pdf. *SKYPER 32PRO R*, 2007.